
STATE-DEPENDENT FORCES IN COLD QUANTUM GASES

Christopher Billington

Submitted in total fulfilment of the requirements
of the degree of Doctor of Philosophy

Supervisory committee:

Prof Kristian Helmerson

Dr Lincoln Turner

Dr Russell Anderson



School of Physics and Astronomy
Monash University

April, 2018

rev: 168 (eb2975e06a08)
author: chrisjbillington
date: Tue Jun 19 17:15:34 2018 +1000
summary: Editing velocimetry

This page intentionally left blank

Contents

Contents	i
2 Atomic physics: Experimental techniques and theory	1
2.1 Cooling, trapping, and manipulating atoms	1
2.1.1 Doppler cooling	1
2.1.2 Magneto-optical and magnetic trapping	2
2.1.3 Optical trapping	2
2.1.4 Polarisation gradient cooling	3
2.1.5 Evaporative cooling	3
2.1.6 Feshbach resonances	4
2.2 Mean field theory: The Gross–Pitaevskii equation and vortices	5
2.3 The ^{87}Rb D line	6
2.3.1 Fine structure	6
2.3.2 Hyperfine structure	7
2.3.3 Zeeman sublevels	10
2.3.4 Putting it all together: the $\{ F m_F\rangle\}$ basis	11
2.3.5 Optical dipole transitions	15
2.3.6 Magnetic dipole transitions	21
2.3.7 Summary	22
5 Particle velocimetry of vortices in Bose–Einstein condensates	23
5.1 Motivation: Turbulence	24
5.2 Overview of velocimetry scheme	26
5.3 Relation to previous work	27
5.4 Sympathetic cooling	28
5.4.1 Model	31
5.4.2 Results	31
5.5 Sisyphus cooling in a 34 G magnetic field	31
5.5.1 Description of cooling scheme	32
5.5.2 Methods	33
5.5.3 Results	35
5.5.4 Vortex-assisted Sisyphus cooling	36
References	39

rev: 168 (eb2975e06a08)
author: chrisjbillington
date: Tue Jun 19 17:15:34 2018 +1000
summary: Editing velocimetry

This page intentionally left blank

rev: 168 (eb2975e06a08)
author: chrisjbillington
date: Tue Jun 19 17:15:34 2018 +1000
summary: Editing velocimetry

CHAPTER 2

Atomic physics: Experimental techniques and theory

BOSE-EINSTEIN CONDENSATES provide such a tantalising opportunity for studying quantum phenomena not only because of their interesting properties, but also because of the level of control they afford, with parameters able to be tuned and manipulated in order to investigate various regimes. Many of the same techniques which allow experimentalists such control over a BEC are also employed in the production of BEC.

The main experimental techniques used to create BEC are Doppler cooling, magneto-optical, magnetic, and dipole trapping, polarisation gradient (Sisyphus) cooling, and evaporative cooling. These were discovered, perhaps by no coincidence, in roughly the same order as they are called for in a BEC experiment, and many were first discovered along the way to the first realisations of Bose–Einstein condensation.

Section 2.1 is a whirlwind summary of these and a few other experimental techniques. Then in section 2.2, I'll present some of the theory describing superfluid flow and vortices and in BEC, which is central to the simulations of vortex tracking presented in chapter 5. The final section of this chapter, section 2.3, will construct the detailed theory for describing the internal state of a ^{87}Rb atom in magnetic and optical fields, considering only the first $L = 0$ to $L = 1$ excitation is accessible to rubidium's sole outer-shell electron. The resulting Hamiltonian describes 32 sublevels, and forms the basis of any detailed calculations of laser cooling and trapping.

2.1 Cooling, trapping, and manipulating atoms

2.1.1 Doppler cooling

Doppler cooling, demonstrated in 1978 [1] is a consequence of the simple observation that atoms see the wavelength of incident light Doppler shifted depending on their velocity. For example, the electric field of a linearly polarised optical plane wave is:

$$\mathbf{E} \propto \cos(\mathbf{k} \cdot \mathbf{r} - \omega t), \quad (2.1)$$

which for an atom moving with constant velocity \mathbf{v} can be written:

$$\mathbf{E} \propto \cos(\mathbf{k} \cdot \mathbf{v}t - \omega t) \quad (2.2)$$

$$= \cos(-\omega_{\text{eff}}t), \quad (2.3)$$

where $\omega_{\text{eff}} = \omega - \mathbf{k} \cdot \mathbf{v}$ is the effective angular frequency of the laser as seen by the atom.

rev: 168 (eb2975e06a08)
author: chrisjbillington
date: Tue Jun 19 17:15:34 2018 +1000
summary: Editing velocimetry

This can be used to selectively transfer momentum to only fast-moving atoms, by tuning an incident laser slightly redder than would be required for a resonant absorption. If six lasers in counterpropagating pairs orthogonal to each other surround a cloud of atoms, the atoms can be cooled close to the *Doppler limit* [2, p 58]

$$k_B T_D = \frac{\hbar\Gamma}{2} \quad (2.4)$$

¹The D₂ line, 5S_{1/2} → 5P_{3/2}, approximately 780 nm.

where Γ is the linewidth of the atomic transition. For the cooling transition used for Doppler cooling ⁸⁷Rb¹, this gives 146 μK, which is approximately a factor of a thousand too high for Bose-condensation. These atoms are also not trapped.

2.1.2 Magneto-optical and magnetic trapping

Magneto-optical trapping, first demonstrated in 1987 [3] comes from the realisation that a magnetic field can be used to *spatially* vary the detuning from resonance that the atoms in the above mentioned arrangement of lasers see. This is possible due to the Zeeman effect [4], in which the wavelengths of atomic transitions are shifted in a magnetic field.

If a field profile can be found which causes the transition to come closer to resonance as the atoms move away from a central point, then it forms a trap—atoms that stray too far from the centre will absorb more strongly and be deflected back².

The field configuration used in an anti-Helmholtz one: two coils opposite each other carrying opposing currents. The resulting magnetic field profile has a zero in the middle and increases in magnitude in all directions.

With the Doppler beams off, this magnetic field still provides a trapping potential, due to the magnetic dipole interaction:

$$V(\mathbf{r}) = -\boldsymbol{\mu} \cdot \mathbf{B}, \quad (2.5)$$

where $\boldsymbol{\mu}$ is the atomic magnetic moment, and \mathbf{B} the magnetic field. This only traps some atomic spin states, and has losses due to spin-flips [5] near the field zero.

The optimal magnetic field gradient for forming a magneto-optical trap (MOT) is lower than that required to merely hold atoms against gravity, and thus there is little if any magnetic trapping occurring in a MOT—the trapping almost entirely results from the position-dependent rate of photon absorption caused by the Zeeman shift due to the magnetic field. To transfer atoms from a MOT to a solely magnetic trap, the magnetic field gradient must be increased substantially.

2.1.3 Optical trapping

Optical trapping on the other hand relies on the *dipole force*, in which off-resonant light shifts the energy of the eigenstates of the combined atom-light system, the so called *dressed states*. This energy shift, called the *light shift*, depends on the intensity of the light, and so results in a potential that spatially varies as the intensity of the light. In the limit of large detuning (compared to Rabi frequency), the resulting energy shift for an atom in a groundstate (the shift for an excited state is the same but with the opposite sign) is [2, p 8]:

$$\Delta E = \frac{\hbar\Omega^2}{4\delta} \quad (2.6)$$

where δ is the detuning from resonance and the Rabi frequency is:

$$\Omega = \frac{E_0}{\hbar} \langle n' | e\hat{r} | n \rangle, \quad (2.7)$$

where E_0 is the amplitude of the light's electric field and $\langle n'|\hat{e}\hat{r}|n\rangle$ is the transition dipole moment between the two states in a two-level system. This transition dipole moment can be either for two specific sublevels coupled by a laser, the calculation of which is detailed in section 2.3.5, or an overall effective transition dipole moment between two manifolds containing many sublevels, if the detuning much larger compared to the spacing between the sublevels.

With the potential proportional to E_0^2 , and thus the light's intensity, the force the atom experiences is proportional to the light's intensity gradient. For this reason, the dipole force is also called the *gradient force*. The name *dipole force* comes from the fact that the force can be equivalently understood to arise from the polarisability of atoms in a light field, giving rise to a force identical to that which traps polarisable materials in optical tweezers [6].

2.1.4 Polarisation gradient cooling

Polarisation gradient cooling, also called Sisyphus cooling, was proposed in 1989 [7,8] to explain experimentally measured cold atom cloud temperatures [9] which, at NIST in 1988, were found to be well below the expected limit obtainable by the well understood method of Doppler cooling³, one of the few examples of experiments turning out better than expected. A one dimensional theory has been developed [7] which has found remarkable agreement with three dimensional experiments [10]

One common configuration for Sisyphus cooling comprises two counterpropagating laser beams in each spatial dimension, both linearly polarised but with their polarisation angles perpendicular to one another. The optical field resulting from the two beams' superposition has regions of linear polarisation and of both helicities of circular polarisation, and varies between them on a length scale shorter than an optical wavelength.

The effect on multi-level atoms as they move from regions of one circular polarisation to another is that they are pumped alternately from one extreme of their spin-projection states to the other, alternately climbing and descending potential hills due to the dipole forces from the regions of different polarisations⁴. And so, like the Greek legend of Sisyphus⁵, who was doomed to push a rock uphill for eternity, the atoms are climbing hills repeatedly. Due to the state dependence of the strength of the dipole forces, the atoms climb steeper hills than they descend, and are thus slowed and cooled.

This type of cooling does not work in a magnetic field; the splitting of transition frequencies makes it impossible for an atom to traverse its spin manifold on one laser frequency. For this reason the Sisyphus cooling stage is performed with magnetic fields off, though a sufficiently short period is required such that the atoms can be recaptured when the trapping field is restored.

2.1.5 Evaporative cooling

The final stage of cooling is forced RF evaporative cooling [11,12], which decreases the temperature of the cloud by systematically removing the hottest atoms. This is performed in a magnetic trap, which as mentioned earlier, only traps certain spin states. Evaporation proceeds by using an *RF knife* to induce spin flips in the atoms. The RF frequency is chosen such that it is only resonant with atoms some distance away from the center of the trap (via the Zeeman shift). The furthest out atoms are the most energetic, possessing the energy to climb the magnetic potential the furthest. By flipping their spins, these atoms are ejected due to the magnetic field becoming anti-trapping for them.

The cloud is given some time to rethermalise and the knife⁶ is moved inward where it removes slightly colder atoms. This is repeated until the desired compromise of lower temperature/lower atom number is reached. Usually some method is employed to prevent atoms near the center of the trap from undergoing spin flips [5] as they move across the

³As well as to explain other discrepancies between experiments and the theory of Doppler cooling, such as the optimal detuning of light being much greater than predicted.

⁴If you consider only one polarisation of light, its intensity varies sinusoidally in space, creating a series of potential hills and wells via the dipole force.

⁵Polarisation gradient cooling is but one of a family of so called 'Sisyphus cooling' methods, all of which involve atoms repeatedly climbing potential hills.

⁶So called because it cuts the tail off the velocity distribution of the atom cloud.

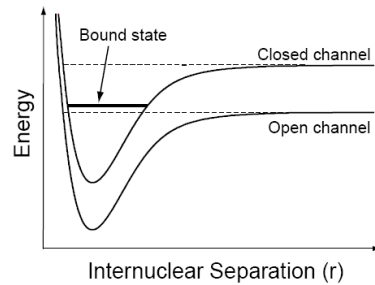


Figure 2.1: When atoms approach each other with spins aligned, they are in the *open channel*. In this channel they are unbound, but do not have enough energy to be free in the other channel - the *closed channel*. In the close range however, the atoms may have energy corresponding to a bound (molecular) state of the closed channel, a resonance which causes a divergence in the scattering length. The energy difference between the two channels can be tuned with a magnetic field and so these resonances can be induced in a wide range of situations.

field zero. The method used in our lab is to use an optical dipole trap in combination with the magnetic trap [13], such that the coldest atoms get trapped in the dipole trap which is offset from the magnetic field zero.

2.1.6 Feshbach resonances

A Feshbach resonance [14] is an enhancement of the interparticle interaction strength when when a certain magnetic field strength is applied⁷. This phenomenon was first discovered in ultracold atoms in 1998 [15], and is now a staple of cold atom experiments.

The interparticle interaction mentioned above:

$$g = \frac{2\pi\hbar^2 a}{m_r} \quad (2.8)$$

where m_r is the reduced mass of a pair of the interacting particles, is dependent on a parameter a called the *s-wave scattering length*, which characterises low energy collisions between atoms. It is sensitive not only to what species of atoms are colliding, but also to their spin states. For each combination of spins, there is a different inter-atomic potential (called a *channel*) which determines the collision dynamics (Figure 2.1).

The resulting scattering length is sensitive to any bound states of this inter-atomic potential which are near the collision energy. If the channels of different spin states are coupled via the hyperfine interaction⁸, then the scattering length is also sensitive to bound states in the channels other than the one the atoms are in when they are far from each other. Due to the Zeeman effect, the energies between the different channels can be shifted with a magnetic field, and so a bound state can be shifted close to the collision energy, which causes the scattering length to diverge.

The end result is that at certain magnetic field strengths we find that atoms are much more strongly attracted to or repelled from each other.

A particular Feshbach resonance of interest is shown in Figure 2.2, and can be used to enhance the interspecies repulsion between ^{87}Rb and ^{41}K . The use of this resonance is assumed for the simulations in chapter 5 to trap tracer particles more strongly in vortex cores of a BEC.

⁷Feshbach resonances can also be induced optically and with RF but magnetic resonances are the most commonly used.

⁸Requiring that the atoms in question have a nuclear magnetic moment.

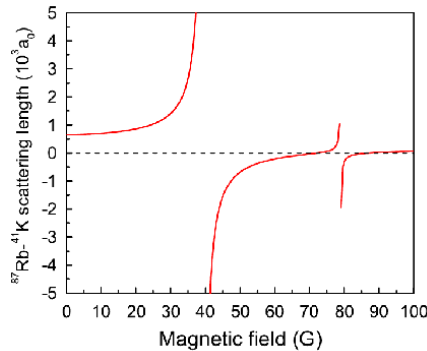


Figure 2.2: Predicted interspecies scattering length [16] as a function of magnetic field strength, for ^{41}K and ^{87}Rb both in their lowest energy hyperfine groundstate. The 35 gauss resonance is one of the main reasons for this pair of atoms being used in this project. It has a particularly low field strength and large width compared to most Feshbach resonances.

2.2 Mean field theory: The Gross–Pitaevskii equation and vortices

Bose-condensates are described well by *mean field* theory, whereby the many-body wavefunction is approximated by a product of identical single-particle wavefunctions. Indeed, that the majority of the atoms are in the same quantum state is one of the defining features of BEC. The effect of interparticle interactions is included as a nonlinear term in the Schrödinger equation for the single particle wavefunctions, known as the Gross–Pitaevskii equation:

$$\frac{\partial \Psi}{\partial t} = \left[-\frac{\hbar^2}{2m} \nabla^2 + V(\mathbf{x}) + g|\Psi|^2 \right] \Psi, \quad (2.9)$$

where g characterises the strength of the interparticle interactions⁹, and $\Psi = \sqrt{N}\Psi_{\text{single}}$ is the single-particle wavefunction scaled by the square root of the number of particles¹⁰.

In the hydrodynamic formulation of quantum mechanics [17], the flow velocity of a spatial wavefunction can be defined by considering the probability current to be a product of density and velocity. This allows us to define the superfluid velocity of a BEC as:

$$\mathbf{v} = \frac{\hbar}{m} \nabla \phi \quad (2.10)$$

where ϕ is the complex phase of the condensate wavefunction Ψ . Integrating this velocity over any closed path γ gives us the circulation:

$$C = \frac{\hbar}{m} \oint_{\gamma} \nabla \phi \cdot d\mathbf{s} \quad (2.11)$$

$$= \frac{\hbar}{m} 2\pi n. \quad n = 0, 1, 2 \dots \quad (2.12)$$

The fact that the circulation is quantised means that vorticity cannot exist in the condensate except in one-dimensional lines, about which the wavefunction's phase winds by a multiple of 2π . These topological defects are the quantised vortices that are central to the vortex tracking simulations in chapter 5.

At a vortex core, the atom density of a BEC must go to zero. This can be intuitively understood to arise from centrifugal forces, but is also required in order for the wavefunction to be continuous and single-valued across the core. This drop in density in the

⁹The nonlinear constant g is usually positive—having the effect of stabilising BECs by self-repulsion.

¹⁰Thus giving it the property that $|\Psi|^2$ is the particle density.

vicinity of a vortex core is exploited by the method simulated in chapter 5 to trap atoms within the cores.

2.3 The ^{87}Rb D line

We atomic physicists do our theory work at an intermediate level of abstraction, at which many quantities and systems of interest can be computed and simulated with accurate models using standard quantum mechanics, but with models that are not fully a-priori. Instead, the Hamiltonians we feed to the machinery of quantum mechanics encapsulate some of the details we are not interested in or that are too hard to compute, with the link between the underlying layers of reductionism and the higher layer usually provided by experimentally measured values rather than calculations from fundamental physics. In this way we can readily compute results about the atoms we are interested in by treating them as simpler systems than they actually are, with some of the underlying details encapsulated by terms in an effective Hamiltonian for the dynamics that we are interested in.

In this section I'll summarise what the ^{87}Rb D line looks like from the perspective of a cold atom physicist, building up a Hamiltonian containing all 32 sublevels of the ground and first excited state of ^{87}Rb including fine structure, hyperfine structure, interaction with a magnetic field, and optical transitions between states. This Hamiltonian is the starting point for any calculations regarding cooling, trapping, and coherent control of ^{87}Rb , and for other alkali earth metals is much the same.

Much of the details of this section are drawn from references [2, 18–21], but the reader should be aware that there are considerable conventional and notational differences between different literature sources. What is presented here is summarised and framed in a way that I think is useful to an experimentalist looking to use the theory to make concrete calculations about real systems.

2.3.1 Fine structure

The rubidium 87 D line refers to the first excitation available to the sole outer electron of ^{87}Rb . Both the ground and excited state of this transition have the same principal quantum number, but different orbital angular momentum quantum numbers. Upon closer inspection, it is not just one transition between a ground state and an excited state—there are two excited states, and the two resulting transitions are called, in order of their transition frequencies, the D₁ and D₂ lines. Thus the ground and first excited state of ^{87}Rb are actually a ground state plus two non-degenerate excited states, once we take into account fine structure. The groundstate is an S state (electronic orbital angular momentum quantum number $L = 0$), called the $S_{1/2}$ state, and the two excited states are P states ($L = 1$), one with the electron spin anti-aligned with its orbital angular momentum (resulting in total angular momentum quantum number $J = 1/2$) and one with the electron spin aligned with its orbital angular momentum ($J = 3/2$), called the $P_{1/2}$ and $P_{3/2}$ states respectively. In all of these states, ^{87}Rb 's single outer-shell electron occupies an orbital with principle quantum number $n = 5$, which for brevity we leave out of the notation. The transition between $S_{1/2}$ and $P_{1/2}$ is called the D₁ line, with experimentally measured (angular) transition frequency ω_{D_1} , and the transition between $S_{1/2}$ and $P_{3/2}$ is the D₂ line with angular transition frequency ω_{D_2} . These transition frequencies correspond to optical wavelengths of $\lambda_{\text{D}_1} \approx 795 \text{ nm}$ and $\lambda_{\text{D}_2} \approx 780 \text{ nm}$ [18].

This fine structure is treated entirely empirically for our purposes, and so our base Hamiltonian for the rubidium D line, taking into account only fine structure, is simply a statement of the experimentally measured energy differences between the states:

$$\hat{H}_{\text{fs}} = \hbar\omega_{\text{D}_2} \hat{1}_{P_{3/2}} \oplus \hbar\omega_{\text{D}_1} \hat{1}_{P_{1/2}} \oplus \hat{0}_{S_{1/2}}, \quad (2.13)$$

where $\hat{1}_{P_{3/2}}$, $\hat{1}_{P_{1/2}}$, and $\hat{0}_{S_{1/2}}$ are identity and zero operators each acting on the subspace of states within the $P_{\frac{3}{2}}$, $P_{\frac{1}{2}}$, and $S_{\frac{1}{2}}$ manifolds respectively, and \oplus is the direct sum.¹¹ The matrix representation H_{fs} of \hat{H}_{fs} in the basis in which it is diagonal (which we will call the $\{|L_J\rangle\}$ basis, since L and J are good quantum numbers¹² for specifying one of the three states, which we write with the spectroscopic notation letter— S or P —corresponding to the value of L in place of its numerical value) is

$$H_{\text{fs}} = \begin{bmatrix} \ddots & & & \\ & \begin{bmatrix} \ddots & \hbar\omega_{D_2} & \ddots \\ & \ddots & \ddots \\ & & \ddots \end{bmatrix} & & \\ & & \begin{bmatrix} \ddots & \hbar\omega_{D_1} & \ddots \\ & \ddots & \ddots \\ & & \ddots \end{bmatrix} & & \\ & & & \begin{bmatrix} \ddots & 0 & \ddots \\ & \ddots & \ddots \\ & & \ddots \end{bmatrix} \end{bmatrix}, \quad (2.14)$$

which is a block-diagonal matrix with each block also being a diagonal matrix. We have not yet specified the size of each submatrix—the size of each differs and depends on how many hyperfine and Zeeman sublevels are in that state.

This base Hamiltonian is worth singling out since the energy differences between its three states are orders of magnitude larger than any of the energy differences between hyperfine and Zeeman sublevels within them. When doing any sort of calculations or simulations then, this time-independent Hamiltonian can often be removed from the equations using an interaction picture (see Section ??), as done in Section 5.5 in simulating laser cooling.

2.3.2 Hyperfine structure

Within each of the $S_{1/2}$, $P_{1/2}$ and $P_{3/2}$ states, the single outer-shell electron's total angular momentum $\hat{\mathbf{J}}$ has an interaction with ^{87}Rb 's nuclear angular momentum $\hat{\mathbf{I}}$. This results in multiple discrete energy levels depending on the relative orientation of the two separate angular momenta. The interaction Hamiltonian for this hyperfine structure is¹³ [18, 22]:

$$\hat{H}_{\text{hfs}} = \frac{A_{\text{hfs}}}{\hbar^2} \hat{\mathbf{I}} \cdot \hat{\mathbf{J}} + \frac{B_{\text{hfs}}}{\hbar^2} \frac{3(\hat{\mathbf{I}} \cdot \hat{\mathbf{J}})^2 + \frac{3}{2}\hat{\mathbf{I}} \cdot \hat{\mathbf{J}} - I(I+1)J(J+1)}{2I(2I-1)J(2J-1)}, \quad (2.15)$$

where J is the total angular momentum quantum number of the electron, equal to either $\frac{1}{2}$ or $\frac{3}{2}$ depending on which state in the D line we are considering, $I = \frac{3}{2}$ is the total angular momentum quantum number of the nucleus, and A_{hfs} and B_{hfs} are empirically determined coupling constants. Here we see the boundary between the quantities we can calculate with the machinery of quantum mechanics and those that we determine empirically—this expression applies so long as J and I are good quantum numbers,¹⁴ and the two terms are the dipolar and quadrupolar interactions [22] between two angular momenta, with the coupling constants determined empirically and encapsulating details that are difficult to compute a-priori, such as relativistic effects and the exact shape of the electron orbitals given the presence of inner shell electrons. For the spherically-symmetric $S_{1/2}$ groundstate, there is no quadrupolar interaction and so B_{hfs} is only nonzero for the two P excited states.¹⁵ The values of A_{hfs} and B_{hfs} for each of the three L_J states of the D line can be found in [18].

For a given state of the D line, we can construct the matrix representation $H_{\text{hfs}}^{I \times J}$ of \hat{H}_{hfs} in the $I \times J$ basis—which we define as the basis in which both the z vector components \hat{I}_z and \hat{J}_z of $\hat{\mathbf{I}}$ and $\hat{\mathbf{J}}$ are diagonal—by constructing matrix representations $\hat{\mathbf{I}}^{I \times J}$ and $\hat{\mathbf{J}}^{I \times J}$ of the operators $\hat{\mathbf{I}}$ and $\hat{\mathbf{J}}$ in that basis and then applying the expression (2.15). The overset $I \times J$ on each of the matrices indicates that the matrix is a representation of its respective operator in the $I \times J$ basis, so named because its basis vectors can be obtained

¹¹Not to be confused with the Kronecker sum, with which it shares notation. The direct sum concatenates matrices as blocks, producing a larger, block-diagonal matrix with dimension equal to the *sum* of the dimensions of the matrices being direct-summed, whereas the Kronecker sum is the regular sum of matrices after each has been multiplied using the Kronecker-product with identity matrices with sizes of the other matrices in the sum, producing matrices with dimension equal to the *product* of those being summed.

¹²A *good quantum number* is a number that can be used to label (not necessarily uniquely) an energy eigenstate, and on which the energy eigenvalue of that state depends. Saying J and L are good quantum numbers is saying that the eigenstates of the overall Hamiltonian are also eigenstates of \hat{L}^2 and \hat{j}^2 , since eigenstates of these two operators can be specified by stating their quantum numbers L and J .

¹³Note that this expression differs from those in the cited references by a factor of $1/\hbar^2$ —this is because I define the $\hat{\mathbf{I}}$ and $\hat{\mathbf{J}}$ angular momentum operators in SI units, rather than in units of \hbar^2 .

¹⁴ J is a good quantum number so long as the hyperfine splitting is small compared to the spacing between the three states of the D line, which it is, and I is a good quantum number so long as the hyperfine splitting is small compared to the energy difference between the groundstate and the first *nuclear* excited state, which it most certainly is.

¹⁵The quadrupolar term should be explicitly excluded from numerical computations of the hyperfine splitting on the $S_{1/2}$ state, as it contains a division by zero in this case, which may lead to erroneous results even if the term is subsequently multiplied by $B_{\text{hfs}} = 0$.

¹⁶The different types of products available for matrices, vectors, operators, spaces, and their sets of basis vectors are rife with subfield-specific conventions and over-loaded notation, leading to much ambiguity. Although ‘Cartesian product’ connotes well what I mean here, it is still ambiguous. What I mean is that the $\mathcal{I} \times \mathcal{J}$ basis is the set of basis vectors $\{\mathbf{u} \otimes \mathbf{v} \mid \mathbf{u} \in \mathcal{I}, \mathbf{v} \in \mathcal{J}\}$. The notation $\mathbf{u} \otimes \mathbf{v}$, which is also ambiguous, denotes the Kronecker product of two column vectors, producing a column vector with number of elements equal to the product of the number of elements in each of the two vectors—not the ‘outer’ or ‘tensor’ product, which would produce a matrix.

¹⁷This explicit procedure for constructing the matrix representations of these operators is useful for entering into a programming language to produce programs capable of performing atomic physics calculations for arbitrary total angular momentum quantum number J , without having to explicitly enter the angular momentum operators for each value of J , which can be tedious and prone to human error.

¹⁸I will hereafter use the terms “ \mathcal{J} basis” and “ $\{|m_J\rangle\}$ basis”, and similarly for other bases, interchangeably, in the understanding that this identification of standard unit vectors with the basis kets is implied.

¹⁹We’re using the standard convention of ordering the eigenkets $\{|m_J\rangle\}$ in descending order of m_J . This is at odds with the computer programming convention of looping over most indices in ascending order, and so care should be taken when constructing these matrices in a computer program.

via a Cartesian product¹⁶ of the two sets of basis vectors from the \mathcal{I} and \mathcal{J} bases for the two individual nuclear and electronic angular momentum degrees of freedom, in which \hat{I}_z and \hat{j}_z are respectively diagonal.

To construct matrix representations of angular momentum operators in the product space basis $\mathcal{I} \times \mathcal{J}$, we first need their matrix representations $\overset{\mathcal{I}}{\mathbf{I}}$ and $\overset{\mathcal{J}}{\mathbf{J}}$ in the bases of their respective subspaces, which we will write as \mathbf{I} and \mathbf{J} for brevity. We can then expand the two operators into the product space by applying a Kronecker product with an appropriate identity matrix to each:

$$\overset{\mathcal{I} \times \mathcal{J}}{\mathbf{I}} = \mathbf{I} \otimes \overset{\mathcal{J}}{\mathbb{I}} \quad (2.16)$$

$$\overset{\mathcal{I} \times \mathcal{J}}{\mathbf{J}} = \overset{\mathcal{I}}{\mathbb{I}} \otimes \mathbf{J} \quad (2.17)$$

where $\overset{\mathcal{I}}{\mathbb{I}}$ is the matrix representation of the identity operator in the \mathcal{I} basis of the nuclear spin degree of freedom, equal to a $(2I + 1) \times (2I + 1)$ identity matrix, with $\overset{\mathcal{J}}{\mathbb{I}}$ defined similarly for the electronic spin degree of freedom.

Each of the two matrices \mathbf{I} and \mathbf{J} is actually a vector of matrices, one for the angular momentum projection in each of the directions x , y and z . The procedure for constructing such matrices for arbitrary total angular momentum quantum numbers is as follows.¹⁷ I’ll show the procedure for constructing J_x , J_y and J_z only for an arbitrary J , the procedure is identical for computing the vector components of \mathbf{I} .

For a given total angular momentum quantum number J , the vector components of \mathbf{J} in the \mathcal{J} basis (the basis in which J_z is diagonal) can be constructed using the raising and lowering operators \hat{J}_+ and \hat{J}_- . Since the action of the raising and lowering operators on an eigenstate of J_z with angular momentum projection quantum number m_J is to produce an adjacent ($m_J \pm 1$) eigenstate multiplied by a constant [23, p 192], this fact can be used to compute the nonzero matrix elements of \hat{J}_+ and \hat{J}_- in the $\{|m_J\rangle\}$ basis (the basis kets of which we identify with the standard basis vectors¹⁸ for a $2J + 1$ dimensional space in order to define the set of concrete basis vectors \mathcal{J}):

$$\langle m_J + 1 | \hat{J}_+ | m_J \rangle = \hbar \sqrt{J(J+1) - m_J(m_J+1)}, \quad -J \leq m_J < J, \quad (2.18)$$

$$\langle m_J - 1 | \hat{J}_- | m_J \rangle = \hbar \sqrt{J(J+1) - m_J(m_J-1)}, \quad -J < m_J \leq J, \quad (2.19)$$

and therefore compute explicit matrices for J_+ and J_- in the $\{|m_J\rangle\}$ basis:¹⁹

$$J_+ = \begin{bmatrix} 0 \langle J | \hat{J}_+ | J-1 \rangle & 0 & \dots \\ \dots & 0 \langle J-1 | \hat{J}_+ | J-2 \rangle & 0 & \dots \\ & \ddots & \ddots & \ddots \\ & \dots & 0 \langle -J+2 | \hat{J}_+ | -J+1 \rangle & 0 \\ & & \dots & 0 \langle -J+1 | \hat{J}_+ | -J \rangle \\ & & & \ddots \\ & & & 0 \end{bmatrix}, \quad (2.20)$$

$$J_- = \begin{bmatrix} 0 & \dots \\ \langle J-1 | \hat{J}_- | J \rangle & 0 \\ 0 & \langle J-2 | \hat{J}_- | J-1 \rangle & 0 & \dots \\ \dots & 0 & \langle J-3 | \hat{J}_- | J-2 \rangle & 0 & \dots \\ & & \ddots & \ddots & \ddots \\ & & \dots & 0 \langle -J | \hat{J}_- | -J+1 \rangle & 0 \end{bmatrix}, \quad (2.21)$$

both of which have nonzero values along only one non-main diagonal adjacent to the main diagonal, and which form a Hermitian conjugate pair (or indeed, a transpose pair, since all elements are real). The matrix representations of \hat{J}_x and \hat{J}_y can then be computed by rearranging the defining expressions for \hat{J}_+ and J_- :

$$\hat{J}_+ = \hat{J}_x + i\hat{J}_y, \quad (2.22)$$

$$\hat{J}_- = \hat{J}_x - i\hat{J}_y, \quad (2.23)$$

rev: 168 (eb2975e06a08)

author: chrisjbillington

date: Tue Jun 19 17:15:34 2018 +1000

summary: Editing velocimetry

for \hat{J}_x and \hat{J}_y , and then applying the result to our matrix representations of \hat{J}_+ and \hat{J}_- to obtain matrix representations J_x and J_y of \hat{J}_x and \hat{J}_y in the $\{|m_J\rangle\}$ basis:

$$J_x = \frac{J_+ + J_-}{2}, \quad (2.24)$$

$$J_y = \frac{J_+ - J_-}{2i}. \quad (2.25)$$

Finally, since $\{|m_J\rangle\}$ is the eigenbasis of J_z with eigenvalues $\{\hbar m_J\}$, the matrix representation of J_z in the \mathcal{J} basis is simply the diagonal matrix of eigenvalues:

$$J_z = \begin{bmatrix} \hbar J & & & \\ & \hbar(J-1) & & \\ & & \ddots & \\ & & & \hbar(-J+1) \\ & & & & -\hbar J \end{bmatrix}. \quad (2.26)$$

We can also construct the matrix representation J^2 of the total (squared) angular momentum operator \hat{J}^2 as

$$J^2 = J_x^2 + J_y^2 + J_z^2, \quad (2.27)$$

or equivalently

$$J^2 = J(J+1)\hbar^2 \mathbb{I}, \quad (2.28)$$

since every m_J state is an eigenstate of the J^2 operator with eigenvalue $J(J+1)\hbar^2$.

The above prescription can be used to produce matrix representations of angular momentum operators J_x, J_y, J_z and J^2 for any integer or half-integer total angular momentum quantum number J . The three components can be considered a vector of matrices, \mathbf{J} , for the vector angular momentum operator $\hat{\mathbf{J}}$. Below is a Python function that computes these matrices as well as the corresponding eigenvectors:

```

1 import numpy as np
2 hbar = 1.054571628e-34
3
4 def angular_momentum_operators(J):
5     """Construct matrix representations of the angular momentum operators Jx,
6     Jy, Jz and J2 in the eigenbasis of Jz for given total angular momentum
7     quantum number J. Return them, as well as the number of angular momentum
8     projection states, a list of angular momentum projection quantum numbers
9     mJ, and a list of their corresponding eigenvectors, in the same order as
10    the matrix elements (in descending order of mJ)."""
11    n_mJ = int(round(J**2 + 1))
12    mJlist = np.linspace(J, -J, n_mJ)
13    Jp = np.diag([hbar * np.sqrt(J*(J+1) - mJ*(mJ + 1)) for mJ in mJlist if mJ < J], 1)
14    Jm = np.diag([hbar * np.sqrt(J*(J+1) - mJ*(mJ - 1)) for mJ in mJlist if mJ > -J], -1)
15    Jx = (Jp + Jm) / 2
16    Jy = (Jp - Jm) / 2j
17    Jz = np.diag([hbar*mJ for mJ in mJlist])
18    J2 = Jx**2 + Jy**2 + Jz**2
19    basisvecs_mJ = [vec for vec in np.identity(n_mJ)]
20    return Jx, Jy, Jz, J2, n_mJ, mJlist, basisvecs_mJ

```

Using the above prescription to construct a matrix representation of the $\hat{\mathbf{J}}$ operator with $J = \frac{1}{2}$ for the $S_{1/2}$ and $P_{1/2}$ states, or $J = \frac{3}{2}$ for the $P_{3/2}$ state, and to construct a matrix representation of the \hat{I} operator with $I = \frac{3}{2}$, we can explicitly construct a matrix representation of the hyperfine interaction Hamiltonian for any state of the ^{87}Rb D line. Remaining is to obtain the matrix representations of the two operators in the $\mathcal{I} \times \mathcal{J}$ product space basis using (2.16) and (2.17), and then we can apply (2.15) to our matrices

```

rev:      168 (eb2975e06a08)
author:   chrisjbillington
date:    Tue Jun 19 17:15:34 2018 +1000
summary:  Editing velocimetry

```

to obtain the matrix representation $H_{\text{hfs}}^{I \times J}$ of \hat{H}_{hfs} for a given J corresponding to one of the three states on the D line:

$$H_{\text{hfs}}^{I \times J} = \frac{A_{\text{hfs}}}{\hbar^2} \mathbf{I} \cdot \mathbf{J} + \frac{B_{\text{hfs}}}{\hbar^2} \frac{\frac{3}{2}(\mathbf{I} \cdot \mathbf{J})^2 + \frac{3}{2}\mathbf{I} \cdot \mathbf{J} - I(I+1)J(J+1)}{2I(2I-1)J(2J-1)}, \quad (2.29)$$

where the products of vector components within the dot products are computed with ordinary matrix multiplication. Alternatively, one can use the matrices in their individual subspaces rather than their equivalents in the product space, so long as one interprets the dot products as “Kronecker dot products”:

$$H_{\text{hfs}}^{I \times J} = \frac{A_{\text{hfs}}}{\hbar^2} \mathbf{I} \circledast \mathbf{J} + \frac{B_{\text{hfs}}}{\hbar^2} \frac{3(\mathbf{I} \circledast \mathbf{J})^2 + 3\mathbf{I} \circledast \mathbf{J} - I(I+1)J(J+1)}{2I(2I-1)J(2J-1)}, \quad (2.30)$$

where \circledast is the Kronecker dot product:

$$\mathbf{I} \circledast \mathbf{J} \equiv I_x \otimes J_x + I_y \otimes J_y + I_z \otimes J_z. \quad (2.31)$$

In the above way one can construct an explicit matrix representation of \hat{H}_{hfs} in the $I \times J$ basis for the hyperfine interaction for a given L_J state of the D line.

Column vectors in the $I \times J$ basis

Because the matrix representations \mathbf{I} and \mathbf{J} of the electron and nuclear angular momentum operators were constructed in the $\{|m_I\rangle\}$ and $\{|m_J\rangle\}$ bases of their respective subspaces, the matrices we have constructed are in the basis $I \times J$ with basis vectors:

$$I \times J = \left\{ |m_I m_J\rangle \mid |m_I\rangle \in \{|m_I\rangle\}, |m_J\rangle \in \{|m_J\rangle\} \right\}, \quad (2.32)$$

where $|m_I m_J\rangle = |m_I\rangle \otimes |m_J\rangle$. The vector representation ψ of a state vector $|\psi\rangle$ in this basis is:

$$\psi = \begin{bmatrix} \langle m_I=I m_J=J | \psi \rangle \\ \langle m_I=I m_J=J-1 | \psi \rangle \\ \vdots \\ \langle m_I=I m_J=-J | \psi \rangle \\ \langle m_I=I-1 m_J=J | \psi \rangle \\ \langle m_I=I-1 m_J=J-1 | \psi \rangle \\ \vdots \\ \langle m_I=-I m_J=-J | \psi \rangle \end{bmatrix}. \quad (2.33)$$

The hyperfine Hamiltonian is not diagonal in the $\{|m_I m_J\rangle\}$ basis. The basis in which it is diagonal—the $\{|F m_F\rangle\}$ basis—will be discussed in section 2.3.4.

2.3.3 Zeeman sublevels

The states differing only in their m_F quantum numbers—called Zeeman sublevels—are degenerate in energy with respect to the hyperfine Hamiltonian, but an external magnetic field lifts this degeneracy. The Zeeman effect [4,18] results in an energy shift proportional to the external magnetic field \mathbf{B} and to a system’s magnetic moment $\boldsymbol{\mu}$:

$$V = -\boldsymbol{\mu} \cdot \mathbf{B}. \quad (2.34)$$

Our atom is a composite particle, made of a nucleus with its own intrinsic magnetic moment, an electron with its own intrinsic one as well, and a contribution from the orbital motion of the electron about the nucleus. Each magnetic moment is proportional to the angular momentum of the subsystem in question, with the proportionality constants,

rev: 168 (eb2975e06a08)
author: chrisjbillington
date: Tue Jun 19 17:15:34 2018 +1000
summary: Editing velocimetry

called Landé g-factors written as dimensionless multiples of $-\mu_B/\hbar$, where μ_B is the Bohr magneton.²⁰ Since J is a good quantum number so long as energy shifts are smaller than the (large) energy spacing between the three L_J states of the D line, on the level we work we don't consider the electron spin and orbital angular momenta separately, rather we encapsulate them with a single, empirically determined Landé g-factor g_J [18] for the magnetic moment of the electron in each of the three L_J states. Similarly we consider the nucleus as a single spin with an experimentally determined g_I [18], resulting in a Zeeman Hamiltonian:

$$\hat{H}_Z = -\hat{\mu} \cdot \mathbf{B} \quad (2.35)$$

$$= -(\hat{\mu}_I + \hat{\mu}_J) \cdot \mathbf{B} \quad (2.36)$$

$$= \left(\frac{g_I \mu_B}{\hbar} \hat{I} + \frac{g_J \mu_B}{\hbar} \hat{J} \right) \cdot \mathbf{B}. \quad (2.37)$$

Separate g_S and g_L values are known and can be used in two terms instead of the one containing \hat{J} above if J is not a good quantum number, but in the regime we work that is not usually the case (and if it were, the fine and hyperfine structure Hamiltonians above would also be inadequate since they assume that J is a good quantum number). If J is a good quantum number then it is more accurate to use the above expression with empirically measured g_J values, since they encapsulate QED effects and corrections due to the multi-electron structure of ^{87}Rb that are not captured by the simple Zeeman Hamiltonian with separate \hat{S} and \hat{L} terms [18].

If the energy shifts from the Zeeman effect are small compared to the hyperfine splitting, then F (the total spin quantum number, defined in the next section) is a good quantum number and a given hyperfine level can be treated as a single magnetic moment subject to the Zeeman Hamiltonian:

$$\hat{H}_{Z\text{lin}} = \frac{g_F \mu_B}{\hbar} \hat{F} \cdot \mathbf{B}, \quad (2.38)$$

where [18]

$$g_F = g_J \frac{F(F+1) - I(I+1) + J(J+1)}{2F(F+1)} + g_I \frac{F(F+1) + I(I+1) - J(J+1)}{2F(F+1)}. \quad (2.39)$$

The direction in which each Zeeman sublevel shifts in energy for small magnetic fields is depicted in Figure 2.3. Experimentally, Zeeman shifts that depart from this linear regime are not infrequently encountered, and so it is an approximation that cannot always be made.

An explicit matrix representation H_Z^J of \hat{H}_Z in the $\{|m_I m_J\rangle\}$ basis for each of the three L_J states of the D line can be constructed by applying (2.37) to the matrix representations of \hat{I} and \hat{J} in that basis:

$$H_Z^J = -\boldsymbol{\mu} \cdot \mathbf{B}, \quad (2.40)$$

where

$$\boldsymbol{\mu} = -\frac{g_I \mu_B}{\hbar} \hat{I}^J - \frac{g_J \mu_B}{\hbar} \hat{J}^J \quad (2.41)$$

$$= -\frac{g_I \mu_B}{\hbar} \hat{I} \otimes \hat{I}^J - \frac{g_J \mu_B}{\hbar} \hat{J} \otimes \hat{J}^J. \quad (2.42)$$

2.3.4 Putting it all together: the $\{|F m_F\rangle\}$ basis

So far we have described how to construct a matrix representation of the fine structure Hamiltonian for the three L_J states of the ^{87}Rb D line, as well as matrix representations of

²⁰We are using the sign convention that defines the Landé g-factor g_J for the electron as positive.

each state's hyperfine and Zeeman Hamiltonians, these latter two in the same $\{|m_I m_J\rangle\}$ basis. In the subspaces of each of the three L_J states then, we can sum together the hyperfine and Zeeman Hamiltonians to form (a matrix representation of) a Hamiltonian that takes interactions into account:

$$\overset{I \times J}{H_{P_{3/2}}} = \overset{I \times J}{H_{\text{hfs} P_{3/2}}} + \overset{I \times J}{H_{Z P_{3/2}}}, \quad (2.43)$$

$$\overset{I \times J}{H_{P_{1/2}}} = \overset{I \times J}{H_{\text{hfs} P_{1/2}}} + \overset{I \times J}{H_{Z P_{1/2}}}, \quad (2.44)$$

$$\overset{I \times J}{H_{S_{1/2}}} = \overset{I \times J}{H_{\text{hfs} S_{1/2}}} + \overset{I \times J}{H_{Z S_{1/2}}}, \quad (2.45)$$

where the subscripts $P_{3/2}$, $P_{1/2}$, and $S_{1/2}$ on the terms on the right hand side indicate that the expressions for the matrix elements of the hyperfine and Zeeman Hamiltonians are to be evaluated using the specific values of J , A_{hfs} , B_{hfs} , and g_J relevant to that state. The total Hamiltonian for the D line including fine structure, hyperfine structure and the Zeeman interaction is then

$$\hat{H} = \hat{H}_{\text{fs}} + (\hat{H}_{P_{3/2}} \oplus \hat{H}_{P_{1/2}} \oplus \hat{H}_{S_{1/2}}) \quad (2.46)$$

$$\Rightarrow \hat{H} = (\hbar\omega_{D_2} \hat{1}_{P_{3/2}} + \hat{H}_{P_{3/2}}) \oplus (\hbar\omega_{D_1} \hat{1}_{P_{1/2}} + \hat{H}_{P_{1/2}}) \oplus \hat{H}_{S_{1/2}}, \quad (2.47)$$

the matrix representation of which in the $\{|L_J m_I m_J\rangle\}$ basis is the block diagonal matrix

$$\overset{I \times J}{H_{D^{87}\text{Rb}}} = \begin{bmatrix} [\hbar\omega_{D_2} + \overset{I \times J}{H_{P_{3/2}}}] & & \\ & [\hbar\omega_{D_1} + \overset{I \times J}{H_{P_{1/2}}}] & \\ & & [\overset{I \times J}{H_{S_{1/2}}}] \end{bmatrix}, \quad (2.48)$$

where addition of scalars with matrices implies the addition of a scalar multiple of the appropriately sized identity matrix.

While $\overset{I \times J}{H_{D^{87}\text{Rb}}}$ is a block diagonal matrix, each of the three submatrices is not diagonal, since m_I and m_J are not good quantum numbers for the hyperfine interaction

(though they are good quantum numbers for the Zeeman interaction and hence $\overset{I \times J}{H_{D^{87}\text{Rb}}}$ becomes approximately diagonal at high magnetic field). Once one has constructed

$\overset{I \times J}{H_{D^{87}\text{Rb}}}$ or its submatrices, there are two other bases one might consider transforming the submatrices into depending on the circumstances. One is the $\Sigma\mathcal{F} = \{|F m_F\rangle\}$ basis²¹, in which the matrix representation of the hyperfine interaction is diagonal. The matrix representation of the Zeeman Hamiltonian is also approximately diagonal in the $\{|F m_F\rangle\}$ basis, so long as one is in the linear Zeeman regime. Furthermore, the transition dipole moments for optical transitions are most easily calculated in the $\{|L_J F m_F\rangle\}$ basis, as we'll see in the next subsection. For these reasons the $\{|F m_F\rangle\}$ basis is the most commonly used and referred to.

The $\{|F m_F\rangle\}$ basis is defined as the simultaneous eigenbasis of the \hat{F}^2 and \hat{F}_z operators, which are the total (squared) and z component of the total angular momentum operator $\hat{F} = \hat{I} + \hat{J}$, the matrix forms F^2 and F_z of which in the $|m_I m_J\rangle$ basis can be

²¹The name $\Sigma\mathcal{F}$ refers to the fact that this is the basis that lends itself to the interpretation of the total space being the direct sum of subspaces, each of which has a well defined F quantum number. So if $I \times J$ is a basis for a product space with $(2I+1) \times (2J+1)$ dimensions, then $\Sigma\mathcal{F}$ is a basis for a sum space with $\sum_i (2F_i + 1)$ dimensions, where F_i ranges from $|I - J|$ to $I + J$ in integer steps. The product and sum bases have the same dimensionality and span the same space, so the difference is only in the identification and composition of their component subspaces.

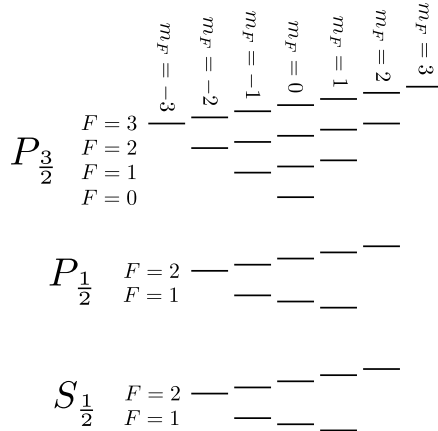


Figure 2.3: The 32 states of the rubidium ^{87}D line, ordered vertically by energy (not to scale) in a small magnetic field. At zero magnetic field, Zeeman sublevels sharing a common F quantum number and within the same hyperfine level are degenerate. At small magnetic fields this degeneracy is lifted, with state energies shifting in the directions depicted. However, F is no longer a good quantum number at nonzero magnetic field, as most of the non-degenerate sublevels are actually equal to linear combinations of two states of different F quantum numbers. Nevertheless at low magnetic fields the states are labelled using F anyway, since one F state dominates the linear combination, and at higher magnetic fields the states are labelled using an index α , equal to the value of F of the state that would dominate the superposition if the field were smoothly reduced to zero. m_F remains a good quantum number at nonzero magnetic field however, and so at all fields a state can be specified by the numbers L, J, α (equal to F at small field) and m_F .

constructed from the matrix forms of the individual angular momentum operators:

$$\begin{aligned} \mathbf{F} &= \mathbf{I} + \mathbf{J} \\ &= \mathbf{I} \otimes \mathbb{I} + \mathbb{I} \otimes \mathbf{J} \end{aligned} \tag{2.49}$$

$$\begin{aligned} \mathbf{F}_z &= \mathbf{I}_z + \mathbf{J}_z \\ &= \mathbf{I}_z \otimes \mathbb{I} + \mathbb{I} \otimes \mathbf{J}_z \end{aligned} \tag{2.50}$$

$$\mathbf{F}^2 = \mathbf{F} \cdot \mathbf{F} \tag{2.51}$$

The $\{|Fm_F\rangle\}$ basis allows the eigenstates of the hyperfine interaction to be labelled with F and m_F quantum numbers. For a state of the ^{87}Rb D line with electron total angular momentum quantum number J , there are $1 + J + I - |(I - J)|$ hyperfine levels, with F quantum numbers running from $|I - J|$ to $I + J$. Within each hyperfine level there are $2F + 1$ degenerate states with different m_F quantum numbers ranging from $-F$ to F . This results in a total of 32 possible states for the rubidium D line, a schematic of which is shown in Figure 2.3.

To transform each submatrix between the $\{|m_I m_J\rangle\}$ and $\{|F m_F\rangle\}$ bases, we use a unitary matrix whose elements are Clebsch–Gordan coefficients, each defined as the inner product of a $|F m_F\rangle$ state with a $|m_I m_J\rangle$ state (written in full as $|I m_I J m_J\rangle$), and

```
rev:    168 (eb2975e06a08)
author: chrisjbillington
date:   Tue Jun 19 17:15:34 2018 +1000
summary: Editing velocimetry
```

calculable as [18]

$$\langle I m_I J m_J | F m_F \rangle = (-1)^{I-J+m_F} \sqrt{2F+1} \begin{pmatrix} I & J & F \\ m_I & m_J & -m_F \end{pmatrix} \quad (2.52)$$

where the object in parentheses is a Wigner 3-j symbol. The Clebsch–Gordan coefficients are real: $\langle F m_F | I m_I J m_J \rangle = \langle I m_I J m_J | F m_F \rangle$, and are zero unless $m_I + m_J = m_F$. Given that the possible range of the F quantum number is from $|I - J|$ to $I + J$, and the possible range of m_F quantum numbers is from $-F$ to F for each F (both in integer steps), an explicit construction of the unitary matrix U_{CG} of Clebsch–Gordan coefficients, in the convention where the column vectors in the $\{|F m_F\rangle\}$ basis have F running from its highest value to lowest from top to bottom, and m_F also running from highest to lowest within each value of F , (omitting I and J for brevity) is:

$$U_{CG} = \begin{bmatrix} \langle m_I=I m_J=J | F=I+J m_F=F \rangle & \dots & \langle m_I=I m_J=J | F=I+J m_F=-F \rangle & \dots & \dots & \langle m_I=I m_J=J | F=|I-J| m_F=-F \rangle \\ \vdots & & \ddots & & & \vdots \\ \langle m_I=-I m_J=J | F=I+J m_F=F \rangle & & & & & \\ \vdots & & & & & \\ \langle m_I=-I m_J=-J | F=I+J m_F=F \rangle & & \dots & & & \langle m_I=-I m_J=-J | F=|I-J| m_F=-F \rangle \\ & & & & & \end{bmatrix}. \quad (2.53)$$

This the matrix that takes vectors from the $\{|F m_F\rangle\}$ basis to the $\{|m_I m_J\rangle\}$ basis, so its Hermitian conjugate U_{CG}^\dagger is needed for the inverse transformation (which is equal to the transpose since the matrix elements are real). Within the convention we're using to order the matrix elements, the vector representation ψ of a state vector $|\psi\rangle$ in the $\{|F m_F\rangle\}$ basis of one of the L_J states is:

$$\psi = \begin{bmatrix} \langle F=I+J m_F=F | \psi \rangle \\ \langle F=I+J m_F=F-1 | \psi \rangle \\ \vdots \\ \langle F=I+J m_F=-F | \psi \rangle \\ \langle F=I+J-1 m_F=F | \psi \rangle \\ \langle F=I+J-1 m_F=F-1 | \psi \rangle \\ \vdots \\ \langle m_F=|I-J| m_F=-F | \psi \rangle \end{bmatrix}. \quad (2.54)$$

Each submatrix of the total Hamiltonian for the D line can be transformed into its $\{|F m_F\rangle\}$ basis by using a unitary matrix of Clebsch–Gordan coefficients with the appropriate value of J , yielding a total Hamiltonian for the rubidium 87 D line in the $\{|J F m_F\rangle\}$ basis:

$$H_D^{87\text{Rb}} = \begin{bmatrix} \left[\begin{smallmatrix} \hbar\omega_{D_2} + U_{CG\ 3/2}^\dagger H_{P_{3/2}} U_{CG\ 3/2} & \overset{I \times J}{\cdots} \\ \cdots & \left[\begin{smallmatrix} \hbar\omega_{D_1} + U_{CG\ 1/2}^\dagger H_{P_{1/2}} U_{CG\ 1/2} & \overset{I \times J}{\cdots} \\ \cdots & \left[\begin{smallmatrix} U_{CG\ 1/2}^\dagger H_{S_{1/2}} U_{CG\ 1/2} & \overset{I \times J}{\cdots} \end{smallmatrix} \right] \end{smallmatrix} \right] \end{smallmatrix} \right] \quad (2.55)$$

$$= \begin{bmatrix} \left[\begin{smallmatrix} \hbar\omega_{D_2} + H_{P_{3/2}} & \overset{\Sigma^F}{\cdots} \\ \cdots & \left[\begin{smallmatrix} \hbar\omega_{D_1} + H_{P_{1/2}} & \overset{\Sigma^F}{\cdots} \\ \cdots & \left[\begin{smallmatrix} H_{S_{1/2}} & \overset{\Sigma^F}{\cdots} \end{smallmatrix} \right] \end{smallmatrix} \right] \end{smallmatrix} \right] \quad (2.56)$$

where the additional subscripts on the unitary matrices indicates the value of J used in its construction. Armed with the $\{|F, m_F\rangle\}$ basis, we have little remaining reason to use the $\{|m_I m_J\rangle\}$ basis any more.

Here is a recap of what we have taken into account with our model of the Rubidium D line:

```
rev:    168 (eb2975e06a08)
author: chrisjbillington
date:   Tue Jun 19 17:15:34 2018 +1000
summary: Editing velocimetry
```

- The two lowest quantum numbers $L = 0$ and $L = 1$ of the electron's orbital angular momentum. This yields the S groundstate and P excited state.
- Fine structure: the two possible orientations of the electron's spin with respect to its orbital angular momentum. This splits the P excited state into two states, $P_{1/2}$ and $P_{3/2}$, and leaves the S groundstate as the single state $S_{1/2}$. The energies of these three states are determined entirely empirically—without any modelling of the fine structure.
- Hyperfine structure: The possible orientations of the electron's total angular momentum with respect to the nuclear angular momentum. This splits each state so far into $1 + J + I - |(I - J)|$ hyperfine states. The hyperfine interaction is treated semi-empirically, using an analytic form of the hyperfine interaction but with empirically determined coupling constants within each of the three L_J states of the D line.
- Zeeman effect: the possible orientation of the angular momenta $\hat{\mathbf{I}}$ and $\hat{\mathbf{j}}$ —or at low field their sum $\hat{\mathbf{F}}$ —onto an external magnetic field. The Zeeman Hamiltonian is modelled analytically, but with empirically determined Landé g factors for each of the three L_J states of the D line.

The above considerations allow us to construct a Hamiltonian, as a concrete matrix representation, for all 32 possible states of the rubidium D line in a fixed magnetic field, in a basis in which it is diagonal for the case of zero magnetic field. In a nonzero magnetic field, one can analytically diagonalise the $S_{1/2}$ and $P_{1/2}$ blocks of this matrix using the Breit–Rabi formula [19, p. 347; 24], but the same cannot be done for the entire D line, and diagonalisation must be performed numerically for the $P_{3/2}$ block. At nonzero magnetic field, F ceases to be a good quantum number, but states are nonetheless labelled using a variable α , defined as the value of F a state *would* have if the magnetic field were reduced to zero. m_F remains a good quantum number however, and thus at nonzero magnetic field the $\{|\alpha m_F\rangle\}$ basis, is the one in which the Hamiltonian is diagonal, with the transformation between it and the $\{|F m_F\rangle\}$ basis requiring numerical diagonalisation.

If the magnetic field is static, then this Hamiltonian $\hat{H}_{\text{D}^{87}\text{Rb}}$ is a time independent Hamiltonian, to which additional time-dependent Hamiltonians can be added to take into account optical or RF transitions, detailed below. In a dynamic magnetic field, only \hat{H}_{hfs} is time-independent, in which case the Zeeman Hamiltonian will also be part of the time-dependent part of the Hamiltonian. This has implications for the use of an interaction picture (described in section ??), in which the time independent part of a Hamiltonian can be analytically removed from the equations of motion, which can make further computations more tractable both analytically and numerically.

2.3.5 Optical dipole transitions

Optical transitions due to laser fields appear as off-diagonal matrix elements in the $\{|F m_F\rangle\}$ basis²². A given laser of a certain polarisation may give rise to nonzero transition matrix elements between several different pairs of states, depending on selection rules.

The potential the outer electron of rubidium is subject to in a classical electric field is the electric dipole potential [2, 19]:

$$\hat{H}_{\text{d}} = -\hat{\mathbf{d}} \cdot \mathbf{E}, \quad (2.57)$$

where \mathbf{E} is the classical electric field and $\hat{\mathbf{d}}$ is the electric dipole operator:

$$\hat{\mathbf{d}} = -e\hat{\mathbf{r}}, \quad (2.58)$$

²²The matrix elements can be obtained in the $\{|\alpha m_F\rangle\}$ basis at nonzero magnetic field via the numerically computed transformation mentioned in the previous subsection

which gives the electric dipole of the atom in terms of the electron's charge $-e$ and its position operator (with respect to the nucleus) $\hat{\mathbf{r}}$. A single matrix element of \hat{H}_d for coupling an initial state $|L_J F m_F\rangle$ to a final state $|L'_J F' m'_F\rangle$ is therefore:

$$\langle L'_J F' m'_F | \hat{H}_d | L_J F m_F \rangle = \langle L'_J F' m'_F | e \hat{\mathbf{r}} \cdot \mathbf{E} | L_J F m_F \rangle, \quad (2.59)$$

which we will abbreviate as

$$\langle n' | \hat{H}_d | n \rangle = \langle n' | e \hat{\mathbf{r}} \cdot \mathbf{E} | n \rangle, \quad (2.60)$$

²³The choice of the symbol n is unrelated to the principal quantum number, which does not vary between the states of the D line.

writing the initial state $|L_J F m_F\rangle = |n\rangle$ and final state $|L'_J F' m'_F\rangle = |n'\rangle$, encapsulating the set of quantum numbers as a single index²³ for the state.

Plane waves

The electric field of a plane wave of amplitude E_0 , polarisation unit vector $\hat{\mathbf{e}}$ and angular frequency ω can be written:

$$\mathbf{E}(\mathbf{r}, t) = \frac{E_0}{2} (\hat{\mathbf{e}} e^{i(\mathbf{k} \cdot \mathbf{r} - \omega t)} + \hat{\mathbf{e}}^* e^{-i(\mathbf{k} \cdot \mathbf{r} - \omega t)}), \quad (2.61)$$

where $*$ is complex conjugation, which in the case of a real valued polarisation unit vector $\hat{\mathbf{e}}$ does nothing, making the above equal to a cosine wave $E_0 \hat{\mathbf{e}} \cos(\mathbf{k} \cdot \mathbf{r} - \omega t)$ as expected for a linearly polarised plane wave. However, (2.61) also allows for arbitrary circular or elliptical polarisation, if $\hat{\mathbf{e}}$ is allowed to have complex components. This comes with the caveat, however, that the amplitude E_0 is a misnomer in these cases and no longer corresponds to any actual amplitude. For example, a circularly polarised plane wave propagating in the z direction constructed using complex polarisation vector $\hat{\mathbf{e}} = \mp(\hat{x} \pm i\hat{y})/\sqrt{2}$ and “amplitude” E_0 actually has an electric field vector with constant magnitude $E_0/\sqrt{2}$. The “amplitude” E_0 in (2.61) is actually equal to $\sqrt{2}E_{\text{rms}}$ and thus only equal to the peak electric field strength in the case of linear polarisation. Using the intensity of the beam²⁴ $I = \epsilon_0 c E_{\text{rms}}^2$ instead, which is less ambiguous and more relatable to experimentalists [20], resolves this potential confusion:²⁵

$$\mathbf{E}(\mathbf{r}, t) = \frac{1}{2} \sqrt{\frac{2I}{\epsilon_0 c}} (\hat{\mathbf{e}} e^{i(\mathbf{k} \cdot \mathbf{r} - \omega t)} + \hat{\mathbf{e}}^* e^{-i(\mathbf{k} \cdot \mathbf{r} - \omega t)}). \quad (2.62)$$

The spherical basis

Consider one of the three polarisation unit vectors $\hat{\mathbf{e}}_q$ for which the photon has a well defined angular momentum projection in the z direction:

$$\hat{\mathbf{e}}_{\pm} = \mp(\hat{x} \pm i\hat{y})/\sqrt{2}, \quad (2.63)$$

$$\hat{\mathbf{e}}_0 = \hat{z}, \quad (2.64)$$

where $q = \pm 1$ is denoted with the subscript \pm . These are the basis vectors of the spherical tensor basis [19], which is the basis in which it is easiest to compute matrix elements, as well as the one in which it is easiest to think about which transitions a given laser will drive. Light with polarisation vector $\hat{\mathbf{e}}_{\pm}$ is called σ^{\pm} polarised, and excites groundstates to excited states that differ in m_F quantum number by ± 1 . A single beam with this polarisation would have to be propagating in the z direction, with left or right hand circular polarisation. Light with polarisation vector $\hat{\mathbf{e}}_0$ is called π polarised, and drives transitions between states of equal m_F quantum numbers. A single beam with this polarisation would have to be propagating with a \mathbf{k} vector in the x, y plane and be linearly polarised in the z direction. However, lasers with propagation directions and polarisation

vectors different from these three configurations can be decomposed into the spherical basis. For example, light with linear polarisation vector in the x, y plane drives both σ^+ and σ^- transitions.

The spherical basis is defined somewhat differently than how we are used to for ordinary real-valued vectors. The components A_q of a vector \mathbf{A} in the spherical basis are defined as the coefficients of *complex conjugates* of the basis vectors:

$$\mathbf{A} = \sum_q A_q \hat{\boldsymbol{\epsilon}}_q^* = \sum_q (-1)^q A_q \hat{\boldsymbol{\epsilon}}_{-q}, \quad (2.65)$$

with the second equality resulting from the property of the basis vectors that

$$\hat{\boldsymbol{\epsilon}}_q^* = (-1)^q \hat{\boldsymbol{\epsilon}}_{-q}, \quad (2.66)$$

and the dot product in terms of the spherical basis components of two vectors is:

$$\mathbf{A} \cdot \mathbf{B} = \sum_q (-1)^q A_q B_{-q}. \quad (2.67)$$

The definition (2.65) has the counter-intuitive consequence that the unit vectors themselves, written in terms of their components $\hat{\boldsymbol{\epsilon}}_q = ((\varepsilon_q)_-, (\varepsilon_q)_0, (\varepsilon_q)_+)$ in the spherical basis are:

$$\hat{\boldsymbol{\epsilon}}_- = (0, 0, -1), \quad (2.68)$$

$$\hat{\boldsymbol{\epsilon}}_0 = (0, 1, 0), \quad (2.69)$$

$$\hat{\boldsymbol{\epsilon}}_+ = (-1, 0, 0), \quad (2.70)$$

that is, the unit vector $\hat{\boldsymbol{\epsilon}}_q$ has a component of $(-1)^q$ in the $-q$ position, and zeros elsewhere.

Considering a plane wave with polarisation vector equal to one of the spherical basis vectors $\hat{\boldsymbol{\epsilon}}_q$, we have the electric field:

$$\mathbf{E}_q(\mathbf{r}, t) = \frac{1}{2} \sqrt{\frac{2I}{\varepsilon_0 c}} (\hat{\boldsymbol{\epsilon}}_q e^{i(\mathbf{k} \cdot \mathbf{r} - \omega t)} + \hat{\boldsymbol{\epsilon}}_q^* e^{-i(\mathbf{k} \cdot \mathbf{r} - \omega t)}), \quad (2.71)$$

which, removing the complex conjugation using (2.66), can be written:

$$\mathbf{E}_q(\mathbf{r}, t) = \frac{1}{2} \sqrt{\frac{2I}{\varepsilon_0 c}} (\hat{\boldsymbol{\epsilon}}_q e^{i(\mathbf{k} \cdot \mathbf{r} - \omega t)} + (-1)^q \hat{\boldsymbol{\epsilon}}_{-q} e^{-i(\mathbf{k} \cdot \mathbf{r} - \omega t)}). \quad (2.72)$$

The dipole approximation

Substituting (2.72) into (2.59) results in the matrix element of the dipole Hamiltonian for a q polarised plane wave:

$$\langle n' | \hat{H}_d(q, I) | n \rangle = \frac{1}{2} \sqrt{\frac{2I}{\varepsilon_0 c}} \left(\langle n' | e \hat{\mathbf{r}} \cdot \hat{\boldsymbol{\epsilon}}_q e^{i(\mathbf{k} \cdot \mathbf{r} - \omega t)} | n \rangle + (-1)^q \langle n' | e \hat{\mathbf{r}} \cdot \hat{\boldsymbol{\epsilon}}_{-q} e^{-i(\mathbf{k} \cdot \mathbf{r} - \omega t)} | n \rangle \right). \quad (2.73)$$

The *dipole approximation* is the approximation that the spatial extent of the electron's orbital is much smaller than the wavelength of the light, and thus that the factors of $e^{\pm i\mathbf{k} \cdot \mathbf{r}}$ are approximately constant over the integral and can be taken outside it, with \mathbf{r} taken to be the expectation value of the atom's position²⁶. For optical wavelengths this is a good

rev: 168 (eb2975e06a08)
author: chrisjbillington
date: Tue Jun 19 17:15:34 2018 +1000
summary: Editing velocimetry

²⁶The resulting classical position \mathbf{r} of the atom should not be confused with the electron's position operator $\hat{\mathbf{r}}$ with respect to the nucleus. Strictly speaking, (2.73) should have \mathbf{r} in the exponents replaced with a quantum operator with a different name to signify that it is the absolute position of the electron rather than the position relative to the nucleus, but I suspect this would cause more confusion than it

approximation, yielding our matrix element in the dipole approximation:

$$\langle n' | \hat{H}_d(q, I) | n \rangle = \frac{1}{2} \sqrt{\frac{2I}{\epsilon_0 c}} \left(\langle n' | e \hat{r} \cdot \hat{\epsilon}_q | n \rangle e^{i(\mathbf{k} \cdot \mathbf{r} - \omega t)} + (-1)^q \langle n' | e \hat{r} \cdot \hat{\epsilon}_{-q} | n \rangle e^{-i(\mathbf{k} \cdot \mathbf{r} - \omega t)} \right). \quad (2.74)$$

Evaluating the dot products using (2.67), we get $\hat{r} \cdot \hat{\epsilon}_q = \sum_p (-1)^p \hat{r}_p (\epsilon_q)_{-p} = \hat{r}_q$ and $\hat{r} \cdot \hat{\epsilon}_{-q} = \sum_p (-1)^p \hat{r}_p (\epsilon_{-q})_{-p} = \hat{r}_{-q}$, where \hat{r}_q are the components of the position operator \hat{r} in the spherical basis, the position space representations of which are proportional to the $\ell = 1$ spherical harmonics and the radial coordinate r :

$$\langle r, \theta, \phi | \hat{r}_\pm | r, \theta, \phi \rangle = \mp \frac{r}{\sqrt{2}} \sin \theta e^{\pm i\phi}, \quad (2.75)$$

$$\langle r, \theta, \phi | \hat{r}_0 | r, \theta, \phi \rangle = r \cos(\theta). \quad (2.76)$$

We now have our final expression for the matrix element $\langle n' | \hat{H}_d(q, I) | n \rangle$ of the dipole Hamiltonian for laser intensity I , angular frequency and wavenumber ω and \mathbf{k} respectively, and complex polarisation vector $\hat{\epsilon}_q$, in the dipole approximation in terms of matrix elements of $e \hat{r}_q$, the calculation of which is detailed below:

$$\langle n' | \hat{H}_d(q, I) | n \rangle = \frac{1}{2} \sqrt{\frac{2I}{\epsilon_0 c}} \left(\langle n' | e \hat{r}_q | n \rangle e^{i(\mathbf{k} \cdot \mathbf{r} - \omega t)} + (-1)^q \langle n' | e \hat{r}_{-q} | n \rangle e^{-i(\mathbf{k} \cdot \mathbf{r} - \omega t)} \right). \quad (2.77)$$

A further approximation often used is to approximate the atom as stationary, replacing the $\mathbf{k} \cdot \mathbf{r}$ from the exponents with a constant (usually zero if the exact phase of the optical field is not of interest). Alternately, if the atom is moving at an approximately constant velocity, the $\mathbf{k} \cdot \mathbf{r}$ term can be absorbed into ω resulting in an effective Doppler-shifted angular frequency as in section 2.1.1. We will leave the $\mathbf{k} \cdot \mathbf{r}$ terms where they are, but note that they are often absent in most literature sources for the preceding reasons.

The rotating wave approximation

If the plane wave's angular frequency ω is close to the resonant angular frequency ω_{D_1} or ω_{D_2} of the D₁ or D₂ line, then one of the two exponential terms is oscillating at a frequency much further from resonance (approximately 2ω) than the other, and thus does not contribute significantly to coupling between states. Discarding it is known as the *rotating wave approximation* (RWA), so called because in an interaction picture (section ??) where the evolution of the base Hamiltonian $\hat{H}_{D^{87}\text{Rb}}$ is factored out—the so called *rotating frame*—this fact is more readily apparent and a formal approximation can be made showing that the off-resonant term averages to zero over time scales much shorter than any other dynamics. Which term is discarded depends on whether the transition being considered is from a groundstate to excited state, or vice-versa. Our matrix element $\langle n' | \hat{H}_d(q, I) | n \rangle$ in the RWA becomes:

$$\langle n' | \hat{H}_d(q, I) | n \rangle \stackrel{\text{RWA}}{\approx} \begin{cases} \frac{1}{2} \sqrt{\frac{2I}{\epsilon_0 c}} \langle n' | e \hat{r}_q | n \rangle e^{i(\mathbf{k} \cdot \mathbf{r} - \omega t)}, & E_{n'} > E_n \\ \frac{(-1)^q}{2} \sqrt{\frac{2I}{\epsilon_0 c}} \langle n' | e \hat{r}_{-q} | n \rangle e^{-i(\mathbf{k} \cdot \mathbf{r} - \omega t)}, & E_{n'} < E_n \end{cases}. \quad (2.78)$$

The spherical basis components \hat{r}_q of the position operator \hat{r} are not Hermitian operators, instead obeying the following relation [19]:

$$\hat{r}_q^\dagger = (-1)^q \hat{r}_{-q}, \quad (2.79)$$

$$\Rightarrow \langle n | e \hat{r}_q | n' \rangle^* = (-1)^q \langle n' | e \hat{r}_{-q} | n \rangle, \quad (2.80)$$

allowing us to simplify (2.78) to:

$$\langle n' | \hat{H}_d(q, I) | n \rangle \stackrel{\text{RWA}}{\approx} \begin{cases} \frac{\hbar}{2} \Omega_{n'n}(q, I) e^{i(\mathbf{k} \cdot \mathbf{r} - \omega t)}, & E_{n'} > E_n \\ \frac{\hbar}{2} \Omega_{nn'}^*(q, I) e^{-i(\mathbf{k} \cdot \mathbf{r} - \omega t)}, & E_{n'} < E_n \end{cases}, \quad (2.81)$$

where $\Omega_{n'n}(q, I)$ is the *Rabi frequency* of the $n \rightarrow n'$ transition for polarisation q and intensity (I),

$$\Omega_{n'n}(q, I) \equiv \hbar \sqrt{\frac{2I}{\epsilon_0 c}} \langle n' | e\hat{r}_q | n \rangle, \quad (2.82)$$

with the symmetry that $\Omega_{n'n}(q, I) = \Omega_{nn'}^*(q, I)$. Because of this symmetry, the electric dipole Hamiltonian for a plane wave in the rotating wave approximation is Hermitian, and all its matrix elements can be computed considering only transitions from groundstate to excited state (with the Rabi frequencies for the reverse transitions being simply the complex conjugates of those of the forward transitions).

The rotating wave approximation is accurate when $\omega - \omega_0 \gg |\omega + \omega_0|$, which is the case for transitions being driven close to resonance. When far off-resonant light is being used however—for example to impart optical dipole forces as in optical traps—it may not be a good approximation, and the full matrix elements (2.77) of the dipole Hamiltonian may need to be considered.

Dipole matrix elements

We now move on to how to compute the dipole matrix elements

$$\langle n' | e\hat{r}_q | n \rangle \equiv \langle L'_J F' m'_F | e\hat{r}_q | L_J F m_F \rangle. \quad (2.83)$$

Using these matrix elements, one can compute Rabi frequencies for matrix elements of the dipole Hamiltonian (2.81) in the rotating wave approximation, or to calculate the full matrix elements (2.77) of the dipole Hamiltonian.

In the spherical basis we've been working in, most of the integrals required to compute these matrix elements can be treated analytically, and there are a series of reductions that can be made to ultimately reduce the matrix elements down to a product of an analytically computable coefficient depending only on angular momentum quantum numbers, and an experimentally measurable ‘reduced’ dipole matrix element.

Following [18], the dependence on the photon angular momentum projection quantum number q and atomic angular momentum projection quantum numbers m_F and m'_F can be encapsulated in a Clebsch–Gordan coefficient using the Wigner–Eckart theorem, allowing us to write:

$$\langle L'_J F' m'_F | e\hat{r}_q | L_J F m_F \rangle = \langle F' m'_F | F 1 m_F q \rangle \langle L'_J F' | e\hat{r} | L_J F \rangle \quad (2.84)$$

$$= (-1)^{F-1+m'_F} \sqrt{2F+1} \begin{pmatrix} F & 1 & F' \\ m_F & q & -m'_F \end{pmatrix} \langle L'_J F' | e\hat{r} | L_J F \rangle, \quad (2.85)$$

where the object in parentheses is a Wigner 3-j symbol, and $\langle L'_J F' | e\hat{r} | L_J F \rangle$ is the ‘reduced’ matrix element for the transition from $|L_J F\rangle$ to $|L'_J F'\rangle$ free of dependence on angular momentum projection quantum numbers. Due to the fact that the Clebsch–Gordan coefficient is zero unless $m_F + q = m_F$, these matrix elements are zero unless the final and initial states are being coupled by a laser of the correct polarisation to conserve angular momentum projection in the z direction, one of the selection rules of optical transitions.²⁷

rev: 168 (eb2975e06a08)
author: chrisjbillington
date: Tue Jun 19 17:15:34 2018 +1000
summary: Editing velocimetry

²⁷Observe equation (2.77) however, and note that for the case of σ^\pm light, both $q = \pm 1$ dipole matrix elements are present, and thus σ^\pm light couples a groundstate to both $m'_F = m_F \pm 1$ excited states, with one being far off resonance and discarded by the rotating wave approximation for the case of near-resonant light.

The final reduction is to express this reduced matrix element as yet another analytic coefficient multiplied by a reduced matrix element that doesn't depend on the F quantum numbers:

$$\langle L'_J | F' | e\hat{r} | L_J \rangle = (-1)^{F+J'+1+I} \sqrt{(2F+1)(2J'+1)} \begin{Bmatrix} J' & J & 1 \\ F & F' & I \end{Bmatrix} \langle L'_J | e\hat{r} | L_J \rangle, \quad (2.86)$$

where I is the nuclear spin quantum number, the object in curly braces is a Wigner 6-j symbol, and $\langle L'_J | e\hat{r} | L_J \rangle$ is a reduced matrix element for the transition from $|L_J\rangle$ to $|L'_J\rangle$ free of dependence on F quantum numbers.

This final reduced matrix element can be linked to experimentally known numerical values via the linewidths Γ_{D_1} and Γ_{D_2} of D₁ and D₂ lines [19, eq. 7.3.7.4]:

$$\Gamma = \frac{\omega_0^3}{3\pi\epsilon_0\hbar c^3} \frac{2J_g + 1}{2J_e + 1} |\langle L'_{J_g} | e\hat{r} | L_{J_e} \rangle|^2, \quad (2.87)$$

where Γ and ω_0 are the linewidth and resonant (angular) frequency respectively of the transition, L'_{J_g} is the groundstate ($S_{1/2}$) and L_{J_e} is the excited state (either $P_{1/2}$ or $P_{3/2}$) of the transition. Thus the reduced matrix elements for transitions from excited to ground-states can be expressed in terms of known constants. For the reduced matrix elements for transitions from ground to excited states instead, one cannot simply take the complex conjugates of the excited-to-ground reduced matrix elements—the reduced matrix elements are defined instead such that they have the following property [19, eq. 7.3.5.1]:

$$\langle L_J | e\hat{r} | L'_J \rangle = (-1)^{J-J'} \sqrt{\frac{2J'+1}{2J+1}} \langle L'_J | e\hat{r} | L_J \rangle^*. \quad (2.88)$$

Putting these together gives the following reduced matrix elements for the D₁ and D₂ lines in both directions:

$$\langle S_{1/2} | e\hat{r} | P_{1/2} \rangle = \sqrt{\frac{3\pi\epsilon_0\hbar c^3\Gamma_{D_1}}{\omega_{D_1}^3}} \quad (2.89)$$

$$\langle S_{1/2} | e\hat{r} | P_{3/2} \rangle = \sqrt{\frac{6\pi\epsilon_0\hbar c^3\Gamma_{D_2}}{\omega_{D_2}^3}} \quad (2.90)$$

$$\langle P_{1/2} | e\hat{r} | S_{1/2} \rangle = \langle S_{1/2} | e\hat{r} | P_{1/2} \rangle^* \quad (2.91)$$

$$\langle P_{3/2} | e\hat{r} | S_{1/2} \rangle = -\frac{1}{\sqrt{2}} \langle S_{1/2} | e\hat{r} | P_{3/2} \rangle^* \quad (2.92)$$

The first two of these, having only their absolute values related to the linewidths and frequencies via (2.87), have an undetermined phase factor which we have taken to be equal to +1. Since only relative phases are important, if we limit ourselves to only one of the D₁ or D₂ lines at a time, all dipole matrix elements, being proportional to these reduced dipole matrix elements, will have the correct relative phases. However, we are imposing a fixed phase on *both* the reduced dipole matrix elements for the D line. We can verify that a relative phase factor of +1 between the two reduced dipole matrix elements is the correct choice by decomposing [18] the reduced matrix elements into yet another Wigner-6j symbol and a reduced dipole matrix element $\langle L' = \frac{1}{2} | e\hat{r} | L = 1 \rangle$, common to both fine structure lines:

$$\langle L'_J | e\hat{r} | L_J \rangle = (-1)^{J+L+S+1} \sqrt{(2J+1)(2L'+1)} \begin{Bmatrix} L' & L & 1 \\ J & J' & S \end{Bmatrix} \langle L' | e\hat{r} | L \rangle, \quad (2.93)$$

where $S = 1/2$ is the electron spin. This expression can be used to verify the ratio:

$$\frac{\langle S_{1/2} | e\hat{r} | P_{3/2} \rangle}{\langle S_{1/2} | e\hat{r} | P_{1/2} \rangle} = \sqrt{2}, \quad (2.94)$$

confirming that the choice of relative phase factor +1 between the two L_J reduced dipole matrix elements is the correct one.

We have now arrived at the ground floor of reductionism for most experimental atomic physicists when it comes to optical transitions, with the values of the transition dipole matrix elements resting on the foundation of empirically measured reduced dipole matrix elements, and calculable by traversing this section in reverse.

2.3.6 Magnetic dipole transitions

After all the complexity of optical dipole transitions, magnetic dipole transitions—for either RF transitions between Zeeman sublevels, or microwave transitions between hyperfine states—are relatively simple. The matrix elements in the $\{|F m_F\rangle\}$ basis for a perturbing magnetic field $\mathbf{B}(t)$ are simply those of the Zeeman Hamiltonian (2.40):

$$\langle F' m'_F | \hat{H}_Z | F m_F \rangle = -\langle F' m'_F | \hat{\mu} \cdot \mathbf{B} | F m_F \rangle, \quad (2.95)$$

which for a magnetic plane wave with linear polarisation $i \in \{x, y, z\}$ and amplitude B_0 , and in the dipole approximation, is:

$$\langle F' m'_F | \hat{H}_Z(i, B_0) | F m_F \rangle = -\langle F' m'_F | \hat{\mu}_i | F m_F \rangle B_0 \cos(\mathbf{k} \cdot \mathbf{r} - \omega t). \quad (2.96)$$

The magnetic dipole matrix elements $\langle F' m'_F | \hat{\mu}_i | F m_F \rangle$ can be computed using the known matrix form (2.41) of the magnetic moment operator μ_i in the $\{|m_I m_J\rangle\}$ basis, and transforming it into the $\{|F m_F\rangle\}$ basis using a unitary of Clebsch–Gordan coefficients as in (2.52).

As with optical dipole transitions, the cosine can be written as a sum of exponentials, revealing co-rotating and counter-rotating terms:

$$\langle F' m'_F | \hat{H}_Z(i, B_0) | F m_F \rangle = -\frac{B_0}{2} \langle F' m'_F | \hat{\mu}_i | F m_F \rangle (e^{i(\mathbf{k} \cdot \mathbf{r} - \omega t)} + e^{-i(\mathbf{k} \cdot \mathbf{r} - \omega t)}), \quad (2.97)$$

allowing for a rotating wave approximation and definition of a Rabi frequency as with optical dipole transitions:

$$\langle F' m'_F | \hat{H}_Z(i, B_0) | F m_F \rangle \stackrel{\text{RWA}}{\approx} \begin{cases} \frac{\hbar}{2} \Omega_{F' m'_F F m_F}(i, B_0) e^{i(\mathbf{k} \cdot \mathbf{r} - \omega t)}, & E_{F' m'_F} > E_{F m_F} \\ \frac{\hbar}{2} \Omega_{F m_F F' m'_F}^*(i) e^{-i(\mathbf{k} \cdot \mathbf{r} - \omega t)}, & E_{F' m'_F} < E_{F m_F} \end{cases}, \quad (2.98)$$

where $\Omega_{F' m'_F F m_F}(i, B_0) = -\hbar B_0 \langle F' m'_F | \hat{H}_Z(i, B_0) | F m_F \rangle$.

The required linear combinations of the above matrix elements can be used to compute matrix elements for RF waves of different phases, or circular polarisations. It is also often practical, when numerically modelling magnetic dipole transitions, particularly between Zeeman sublevels, to simply include the magnetic field vector as a function as time and evaluate the entire matrix H_Z directly in whichever basis one is working, rather than decomposing it into fixed frequency waves. This is particularly useful for frequency sweeps and other complex magnetic field sequences, which may not be good candidates for the rotating wave approximation, or may not be well represented well as single-frequency waves at all. This is most practical for transitions between Zeeman

sublevels, since the energy splittings can be on the order of MHz and therefore well sampled by numerics with nanosecond to microsecond sized timesteps, which are feasible to numerically compute. Microwave transitions, being 6.8 GHz in ^{87}Rb would require sub-nanosecond timesteps to simulate in this direct way, and so is more taxing but still within the range of possibility, as opposed to optical transitions which are in the hundreds of THz and impractical to simulate without rotating wave approximations and the assumption of monochromatic waves as treated in the previous subsection.

2.3.7 Summary

We are now finally at the end of our assembly of the Hamiltonian for the ^{87}Rb D line in the presence of magnetic fields and monochromatic plane waves. Armed with this Hamiltonian and the ability to compute its coupling terms for various lasers, the atomic physicist can predict and simulate much of what is needed for the basics of laser cooling, trapping, and coherent control.

rev: 168 (eb2975e06a08)
author: chrisjbillington
date: Tue Jun 19 17:15:34 2018 +1000
summary: Editing velocimetry

Particle velocimetry of vortices in Bose–Einstein condensates

THIS CHAPTER INVESTIGATES, via numerical simulation, an imaging method for the real time tracking of quantum vortices in a turbulent ^{41}K condensate. The method involves ultracold ^{87}Rb tracer particles that become bound to vortex lines in the condensate and are imaged continuously to track the vortex lines as they move. The imaging of tracer particles to track vortex motion has previously proved successful in superfluid helium [25–27], and the method of laser cooling and imaging atoms in high resolution with the same laser light has also been successful in cold atom systems [28]. This chapter presents the results of numerical simulations of the method under a number of assumptions to establish its feasibility as an imaging method.

This method has the potential to overcome several existing difficulties that typical imaging techniques face when used to image vortices. In ordinary absorption imaging, atoms are imaged via resonant absorption of the condensate itself, and vortices—visible as density minima—generally can only be seen when the vortex line is normal to the image plane. If not viewed end-on in this way, a vortex line represents only a minor decrease in column density and cannot be distinguished from the rest of the condensate (Figure 5.1). One solution to this problem is to slice the condensate into layers, and image

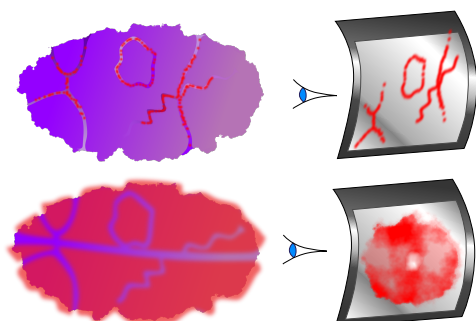


Figure 5.1: Imaging of the condensate itself, whether by fluorescence (bottom) or absorption imaging makes it difficult to resolve vortices unless they are viewed end-on. The vortex cores are usually smaller than the imaging light’s wavelength, and are thus also difficult to resolve unless the cloud is allowed to expand. Imaging tracer particles instead (top) has the potential to resolve both these problems.

them separately [29].

The use of tracer particles that are only present within vortex cores allows vortex lines to be visible from any viewing angle. Furthermore, since the atoms being imaged reside in the vortex cores themselves rather than the bulk of the condensate, this imaging can potentially be repeatedly or continuously performed without destroying the condensate. This may enable observation of the time evolution of Kelvin waves [30], vortex reconnections [31], and vortex rings [29].

This *in-situ* imaging of vortex dynamics may allow more types of vortex motion to be imaged. Dynamics of BECs are typically studied using a shot-by-shot method, in which repeated experiments with identical initial conditions are imaged destructively after being allowed to evolve for different amounts of time. Whilst this works for many types of dynamics, it fails for experiments that are sensitive to initial conditions and noise (quantum or otherwise), such as turbulent flow. This includes phenomena which cannot be created reliably in the same initial state, even though the evolution thereafter would be consistent from one experimental run to the next. One such phenomenon is the spontaneous generation of vortices after evaporative cooling [32].

In-situ imaging of vortex motion has been achieved previously [33], by ejecting a fraction of the atoms from the condensate periodically and imaging them. This process is limited by depletion of the condensate, and was also used only to image vortices end-on. The fraction of the condensate being imaged was also allowed to freely expand before being imaged, since vortex cores are otherwise unable to be resolved by the wavelength of light used. Our proposed method would require neither free expansion or depletion of the condensate.

5.1 Motivation: Turbulence

It is commonly said that turbulence is one of the greatest unsolved problems of classical physics. But in what sense is it an unsolved problem? It is not a problem at all if your aim is reductionism—the Navier–Stokes equation adequately describes the evolution of a Newtonian fluid within its domain of validity, and the process of deriving it from the underlying motion of classical particles is well understood. It's turtles all the way down [34, p 1]; what more could we ask for?

A demonstrative comparison might be with the field of thermodynamics, as precisely the same statement can be made about the energy content and exchange between systems of particles. Thermodynamics has revealed that despite the chaotic motion of individual particles in an ensemble, definite statements can still be made about the behaviour of the system as a whole, *without having to consider the dynamics of the constituent components in detail*.

This is the kind of solution people have in mind when they speak of ‘solving’ the problem of turbulence. Laws describing the average properties of a fluid without reference to its precise flow field would not simply be interesting as describing turbulence as an emergent phenomenon, but would aid practical computations, which for many problems of interest are prohibitively computationally expensive. The flow of a turbulent fluid contains detail on such a wide range of length scales that finite-element or finite-difference analyses of a system such as an aeroplane wing requires a very high resolution in order to be accurate. Following an estimate of computing power required to simulate a turbulent system down to its smallest length scales, Stanley Corrsin quipped [35]:

The foregoing estimate is enough to suggest the use of analog instead of digital computation; in particular, how about an analog consisting of a tank of water?

The reliance of the aerospace industry on wind tunnels and practical tests shows that there is some truth to the necessity of using nature as one's computer when it comes to turbulence. Whilst nature must always have the final say, it would be of great benefit to be able to compute expected results more cheaply before setting up a wind-tunnel experiment or constructing a prototype aircraft.

But are we asking for too much? Perhaps the statistical properties of a turbulent fluid fundamentally cannot be decoupled from the finer details. There is reason to believe that this is not the case. There are several tantalising results that hint at universal properties that all turbulent flows share, and there is the simple empirical observation that the average flow of turbulent fluids at large scales is reproducible from one experimental run to the next [36, pp 13, 86].

One of these universal results is Kolmogorov's theory of the statistics of small eddies [37, 38]. Another is the fact that the rate of energy dissipation via the action of viscosity at small scales is independent of the viscosity itself [36, p 77].

Then there is the Richardson energy cascade [39], in which energy is continually transferred from larger scales to smaller scales. With dissipation at the smallest scales and addition at larger scales, this allows for the existence of 'steady state' turbulence.

The above examples derive from ordinary, viscous fluids. Bose–Einstein condensates on the other hand are superfluids. There are several interesting aspects of superfluid turbulence that differ from classical turbulence. The defining difference is the absence of viscosity; another major difference is the quantisation of circulation. On length scales much larger than spacing between vortex lines, superfluid turbulence is expected to closely resemble classical turbulence [40]. At smaller scales however the energy dissipation mechanism is different, instead involving the production of sound waves via vortex interactions [40, 41].

In certain 2D geometries, an *inverse cascade* [42, 43] is predicted to take place in superfluids, whereby energy moves not from large scales to small, but from small to large, clustering quantised vortices of the same circulation direction together. This phenomenon has been studied theoretically and numerically in the Monash Quantum Fluids group [44, 45] and recently experimentally observed in the Monash Dual-Species laboratory in experiments performed by Shaun Johnstone [46], simultaneously with a group at the University of Queensland [47].

The following definition of turbulence, taken from [36, p 53], emphasises the role of vortices in turbulence in general:

Incompressible hydrodynamic turbulence is a spatially complex distribution of vorticity which advects itself in a chaotic manner in accordance with [the vorticity equation¹]. The vorticity field is random in both space and time, and exhibits a wide and continuous distribution of length and time scales.

When vorticity exists only in infinitely narrow lines, as it does in superfluid, the vorticity equation mentioned in the above definition reduces to a Biot–Savart type law which can be used to compute the motion of vortices without having to compute the entire flow field.

This is why we are interested in the study of the dynamics of quantised vortices. Unlike in classical fluids, the vortices in superfluids have a definite position and size; there is either a vortex at a given spatial location or there is not. This may make it simpler to describe the motion of vortices statistically.

So far experimental studies of superfluid turbulence have been primarily in the context of liquid helium [48]. Bose–Einstein condensates offer a compelling alternative subject of study for superfluid turbulence. The high degree of control afforded over systems of cold atoms allows the superfluid's properties to be tweaked in several ways, creating a larger parameter space in which to study turbulence than that afforded by liquid helium.

¹Which is a transformation of the Navier–Stokes equation for an incompressible fluid into a form in which the vorticity field is center-stage.

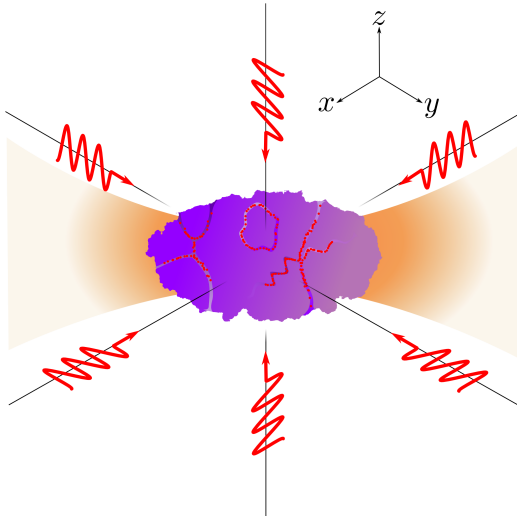


Figure 5.2: The simplest scheme for cooling and imaging the tracer particles with the same light is polarisation gradient cooling, involving six slightly off resonant beams (red), with each counterpropagating pair having opposite linear polarisations. This will scatter some light off the tracer atoms, as well as cool them to sub-Doppler temperatures. If the cooling is sufficient, it should encourage the atoms into the vortex cores where their energy is lower, if they aren't already there. Both the rubidium tracers and the potassium BEC will be trapped with approximately the same trapping potential by a strong, far off-resonant laser (orange), via the dipole force. Magnetic trapping cannot be used, as polarisation gradient cooling does not work in the presence of a magnetic field.

5.2 Overview of velocimetry scheme

As mentioned, the core idea of our proposed imaging method is to use tracer particles to track vortex cores in a BEC in real time. In this chapter I consider ^{87}Rb atoms as tracer particles in a BEC made of ^{41}K . This choice is due to the strong interspecies repulsion between these atomic species, which gives rise to the trapping of atoms in the vortex cores. In the limit of low densities and temperatures, such that three body collisions are suppressed and s-wave scattering dominates the interspecies interactions [49, p 120], the rubidium tracer atoms experience a potential due to the potassium:

$$V(\mathbf{r}) = \frac{2\pi\hbar^2 a_s}{m_r} \rho_{\text{K}}(\mathbf{r}), \quad (5.1)$$

where $\rho_{\text{K}}(\mathbf{r})$ is the spatially varying atom density of the potassium condensate, a_s is the interspecies s-wave scattering length, and $m_r = \frac{m_{\text{K}} m_{\text{Rb}}}{m_{\text{K}} + m_{\text{Rb}}}$ is the reduced mass of the scattering pair. Vortex cores thus create potential wells for other atoms, since they are regions of low condensate density in a background of high density.

The basic setup of the scheme is shown in Figure 5.2. Cold rubidium atoms are introduced (such as by magnetic transport from a MOT) to a potassium condensate, after which both species are optically trapped at the focus of a high power 1064nm laser, using the dipole force. Various methods may be used to create vortices in the condensate. These include bluff-body flow, where a repulsive potential is dragged through the condensate, and inducing a turbulent state by applying off-resonant laser speckle. The rubidium atoms are then expected to become trapped in the low density vortex cores.

rev: 168 (eb2975e06a08)
author: chrisjbillington
date: Tue Jun 19 17:15:34 2018 +1000
summary: Editing velocimetry

The atoms are imaged with resonant or near-resonant laser light, depending on the exact scheme employed. In this chapter I present the results of simulating two configurations, one of which has near-resonant laser light also cooling the atoms to keep them trapped in the vortex cores, and the other relying solely on sympathetic cooling with imaging being performed with resonant light.

The simplest scheme which attempts to cool the rubidium atoms is ordinary polarisation gradient cooling, in which the same light is used for imaging and cooling the atoms (Figure 5.2). This was considered in my Honours thesis [50], the results of which I summarise in the next section. This method precludes the use of a magnetic trap or large bias field, since either would destroy the cooling effect.

The vortex potentials may be made deeper through the use of a Feshbach resonance (Section 2.1.6), which increases the interspecies scattering length. However, since this requires a magnetic field, it precludes the use of ordinary polarisation gradient cooling. In section (see Section 5.5) I present an alternative polarisation gradient cooling scheme designed work in the presence of a magnetic field of the strength required for the Feshbach resonance of interest.

Effective imaging of vortex motion would require approximately 10^5 photons per second to scatter off each rubidium atom without it escaping its vortex core trap, and without causing so much heating as to destroy the condensate on a reasonable experimental timescale. A high resolution, low aberration lens (numerical aperture ≈ 0.5) would also be required to focus the scattered light onto a fast capture, high quantum efficiency camera to produce images of vortex motion.

5.3 Relation to previous work

This scheme was first investigated in my Honours project [50]. In that work I investigated the ability of vortex potentials to trap atoms, including consideration of the depth of such traps when measured in units of the photon recoil energy. Considering the depth in these units was a first attempt to estimate how easily atoms may escape vortex potentials in the presence of imaging light. Figure 5.3 and Figure 5.4 show bound states of typical vortex potentials at different condensate densities.

There were a number of conclusions from this investigation. Firstly, to minimise the recoil energy, rubidium is a better choice for tracer particle than potassium due to its larger mass, enabling a rubidium atom to remain trapped after scattering a number of photons that would cause a potassium atom to escape the same potential. Secondly, vortex potentials are not very deep when measured in recoil energies, and their depth depends strongly on the density of the BEC. At typical condensate densities of 10^{14} cm^{-3} , the vortex potentials are expected to only be one or two recoil energies deep, making it unlikely that atoms could scatter many photons whilst remaining trapped in them. At larger densities of 10^{15} cm^{-3} , the vortex potentials are closer to 20 recoil energies deep, making imaging of trapped tracer atoms more plausible.

The main simulation result of my Honours project considered a potassium condensate with a peak density of 10^{15} cm^{-3} and rubidium tracer atoms being cooled using standard polarisation gradient cooling with parameters chosen to ensure each atom scattered 10^5 photons per second in two spatial dimensions. The result was that initially randomly distributed rubidium atoms were able to become and remain trapped in the vortex cores whilst being cooled (Figure 5.5).

However, the density assumed in this simulation was rather high for a real experiment. Three-body losses tend to limit the lifetime of condensates at such a high density, and so the work in this chapter investigates ways to make particle velocimetry work in a less dense condensate. As the vortex potentials are so shallow at lower density, as mentioned earlier the potentials may be deepened through the use of a Feshbach resonance.

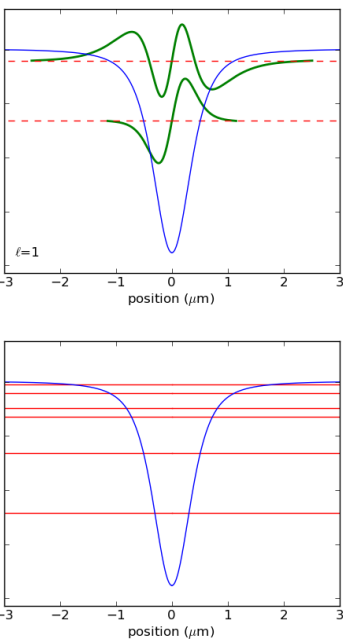


Figure 5.3: Energy eigenstates of a rubidium atom in a potassium vortex core, for a potassium BEC with background density $\approx 10^{14} \text{ cm}^{-3}$. There are a number of bound states spanning three orbital quantum numbers. Plots of the bound states are of a cross section through the centre of a vortex core, and the lower right plot shows just the energy levels. Figure reproduced from [50].

In Section 5.4 I consider a similar configuration, but with a more reasonable BEC density combined with an enhancement of the interspecies repulsion due to a Feshbach resonance. I investigate whether sympathetic cooling of the tracer atoms by the condensate may be enough to keep them trapped in the presence of imaging light. Then, in Section 5.5 I present simulation results of a new laser cooling scheme designed to work at the magnetic field strength required for the Feshbach resonance.

5.4 Sympathetic cooling

The simulation performed in my Honours thesis considered only polarisation gradient cooling counteracting the heating effect of the imaging light. In reality, collisions between tracer atoms and atoms in the condensate would also contribute to cooling. This sympathetic cooling of the tracer atoms—which would also lead to heating of the condensate—was disregarded in my Honours thesis’ results.

Depending on the strength of the cooling effect from sympathetic cooling, this cooling may be sufficient to retain tracer atoms in vortex cores in the absence of an additional cooling mechanism such as polarisation gradient cooling. If laser cooling is not necessary to trap tracer atoms in vortices, then the Feshbach resonance may be used to enhance the interspecies scattering length, further enhancing the ability of the vortices to trap tracer atoms. In this section I consider a similar simulation to that in my Honours thesis, in which the tracer atoms are subject to sympathetic cooling only, in order to examine this possibility.

```
rev:    168 (eb2975e06a08)
author: chrisjbillington
date:   Tue Jun 19 17:15:34 2018 +1000
summary: Editing velocimetry
```

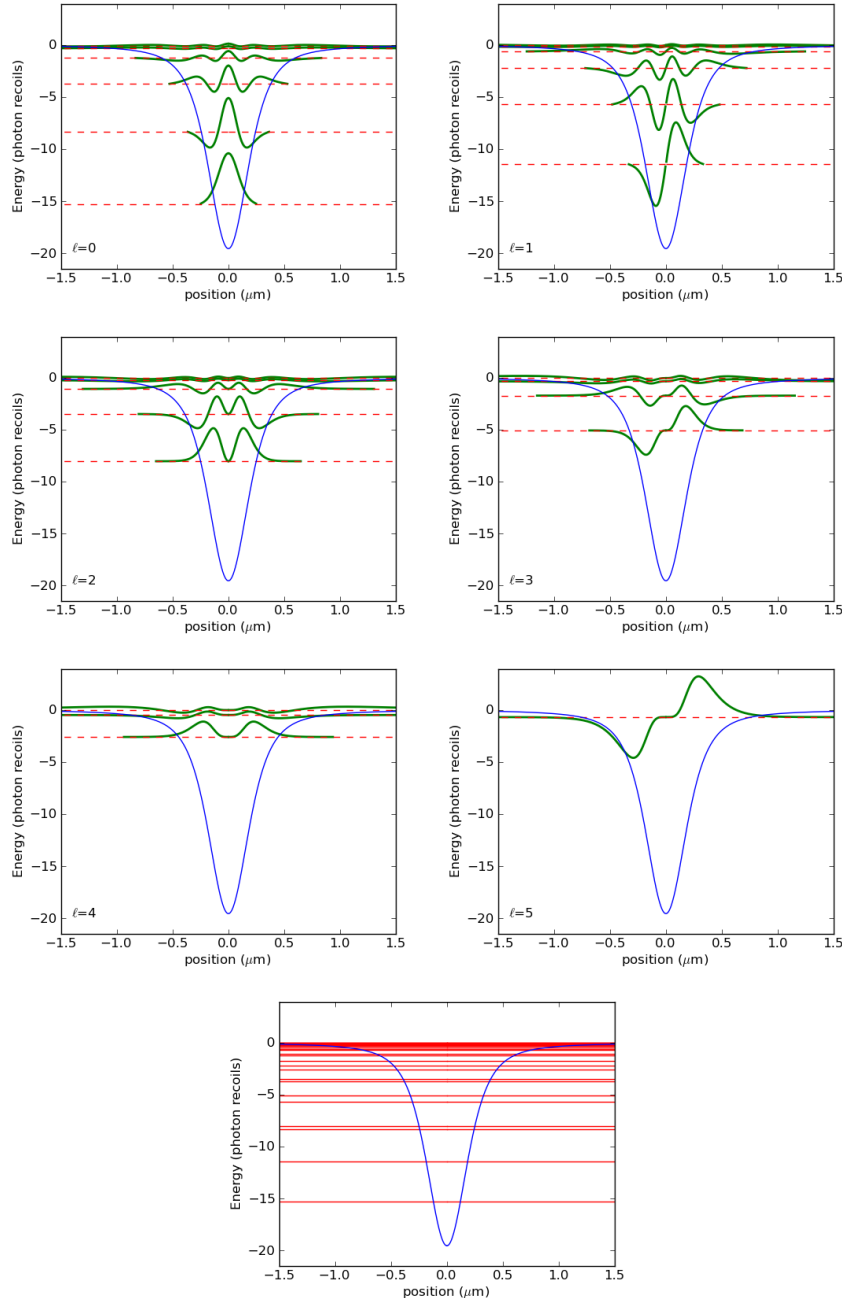


Figure 5.4: As in Figure 5.3, but for a potassium BEC with background density $\approx 10^{15} \text{ cm}^{-3}$. There are bound states over six different orbital quantum numbers. This vortex potential is much deeper than that in Figure 5.3, showing the effect of condensate density on the depth of the vortex potentials. Figure reproduced from [50].

```

rev:    168 (eb2975e06a08)
author: chrisjbillington
date:   Tue Jun 19 17:15:34 2018 +1000
summary: Editing velocimetry

```

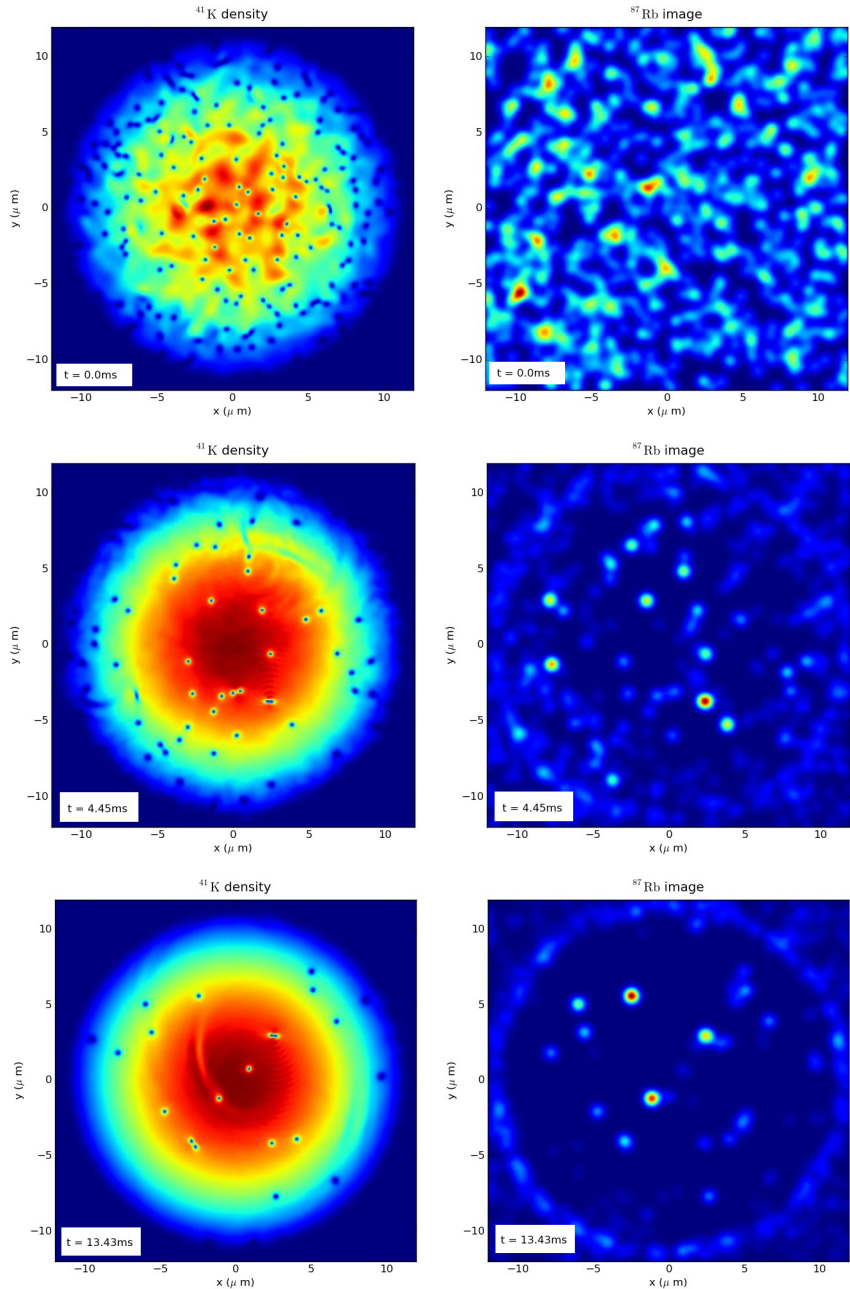


Figure 5.5: The result from [50] of a two-dimensional hybrid quantum-classical simulation for 1000 classical rubidium atoms (right, depicted as fluorescence assuming diffraction through an NA = 0.5 imaging system) and a turbulent potassium BEC (left) of peak density $\approx 10^{15} \text{ cm}^{-3}$. The rubidium atoms are subject to a classical approximation of the force due to polarisation gradient cooling as described in [50]. Most rubidium atoms eventually either become bound to a vortex core or leave the condensate. Figure reproduced from [50].

rev: 168 (eb2975e06a08)
author: chrisjbillington
date: Tue Jun 19 17:15:34 2018 +1000
summary: Editing velocimetry

5.4.1 Model

As with the simulation in my Honours thesis, in this section I model the tracer particles classically in a BEC

In this section I model sympathetic cooling due to elastic two-body scattering between the rubidium tracer atoms and the potassium atoms in the condensate. The model is two-dimensional, approximating a pancake-shaped condensate.

The potassium condensate is modelled with the Gross–Pitaevskii equation:

[BLAH]

where [define symbols], and the rubidium atoms follow the classical equation of motion

[blah]

where [define symbols].

The motion of the tracer atoms is punctuated by velocity jumps due to scattering of imaging photons and to two-body collisions with the condensate. The effect of photon scattering is modelled as velocity jumps of magnitude [RECOIL MOMENTUM EQUALS EXPRESSION] in a random direction projected into the 2D plane [VERIFY] of the simulation, occurring at random times at an average rate given by the photon scattering rate. The latter modelled as elastic collisions between a rubidium atom with the given classical velocity, and a potassium atom of velocity equal to the superfluid velocity [SYMBOL] of the condensate at the location of the tracer atom:

[EXPRESSION FOR SUPERFLUID VELOCITY]

The rate of two body collisions is given by the scattering cross section times the relative velocity or something like that:

[EXPRESSION]

Where the scattering cross section is - uh, check how I calculated it, it involves a Feshbach resonance obviously. At low temperatures *s*-wave scattering dominates so we're just using that.

5.4.2 Results

DEFINE EVERYTHING TURBULATE INITIAL CONDITIONS, REFER TO NUMERICS SECTIONS

5.5 Sisyphus cooling in a 34 G magnetic field

As mentioned, one of the limitations of the usual method of polarisation gradient cooling is that it doesn't work in a magnetic field. Usually this is not an issue for the cooling stage used en-route to BEC; the magnetic field is simply temporarily switched off. Our imaging method would benefit from a cooling scheme that does work in a magnetic field, since the repulsive interactions between ^{87}Rb and ^{41}K can be greatly enhanced via a Feshbach resonance at 34 G [16]. This would make the potential wells that the rubidium atoms see deeper, trapping them more strongly. However if the magnetic field destroys the cooling mechanism then the atoms won't stay trapped for long. Even if sympathetic cooling is sufficient to image tracer particles trapped in vortices, the addition of a cooling scheme would increase the lifetime of the condensate on account of decreased sympathetic heating, and may allow a larger scattering rate of photons before the tracer atoms cease to be trapped.

The Feshbach resonance only occurs if both species are in their respective $|F = 1, m_F = 1\rangle$ spin state,² so a cooling mechanism in which the rubidium atoms spend a significant fraction of their time in this state is desirable.

In this section I present a sub-Doppler cooling scheme that is designed to cool ^{87}Rb in a 34 G magnetic field. The basic Sisyphus mechanism—of atoms moving alternately

² F is not a good quantum number in a nonzero magnetic field, so what we mean writing this is the state that one would get if starting in an F state and adiabatically turning on the magnetic field.

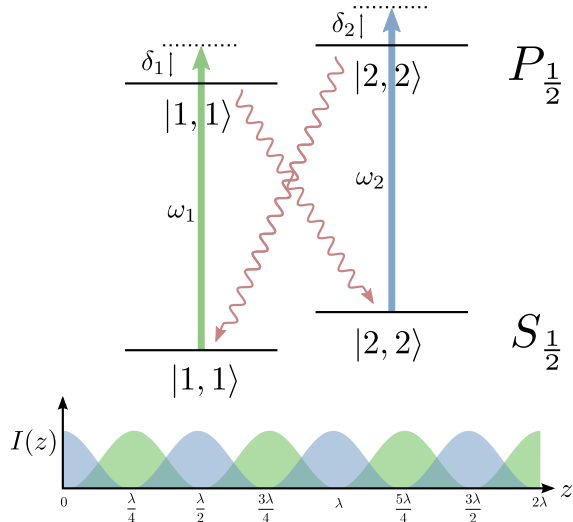


Figure 5.6: An idealised depiction of the cooling scheme, with repump lasers and undesired states not shown. Two lasers on the D_1 line are used for cooling, both linearly polarised, and arranged so as to form two interleaved standing waves. Both are blue detuned from the transitions they target, and they differ by about 6.8 GHz. This difference means that the alignment of the two standing waves can only be maintained over a distance of about a centimetre.

³And indeed, many other Sisyphus cooling mechanisms exists other than polarisation gradient cooling [2, p 116].

between spin states which see different potentials—is possible to find in many multi-level systems of sufficient complexity³; my cooling scheme uses a Sisyphus mechanism with four lasers to cool and repump ^{87}Rb atoms in a 34 G field, with the atoms spending approximately half their time in the $|1, 1\rangle$ state.

In Section 5.5.4, I briefly describe another cooling scheme suggested by Kris Helmer son, which uses the vortex cores themselves as the potential hills in a Sisyphus mechanism. I have not simulated this scheme to asses its viability; I mention it here because it is illustrative of the type of problem that is difficult to model semiclassically, and was one of the factors that led me to consider the use of hidden variables in semiclassical models, as discussed in Chapter ??.

5.5.1 Description of cooling scheme

The scheme involves four lasers, two for cooling and two for repumping. For simplicity I will first focus on the cooling lasers only, depicted in Figure 5.6. Consider a rubidium atom at $z = 0$ and in the $|1, 1\rangle$ hyperfine groundstate. At this position the atom sees no light, as the intensity of the cooling laser labelled ω_1 is zero, and it is in the wrong state to be pumped by the ω_2 laser (which is not resonant with any transitions from the $|1, 1\rangle$ groundstate).

As the atom moves rightward however, it will have to climb the repulsive potential hill formed by the ω_1 laser. As it does so, its $|1, 1\rangle$ excited state probability will increase, and along with it, the probability of spontaneous emission. Spontaneous emission will be most likely to occur near the top of the potential hill where the laser intensity—and hence the excited state probability—is greatest.

The most likely groundstate for the atoms to decay to from the $|1, 1\rangle$ excited state is the $|2, 2\rangle$ groundstate, and this is most likely to occur near $z = \frac{\lambda}{4}$. If this occurs, we now have an atom in the $|2, 2\rangle$ groundstate at $z = \frac{\lambda}{4}$, a situation similar to that in which it

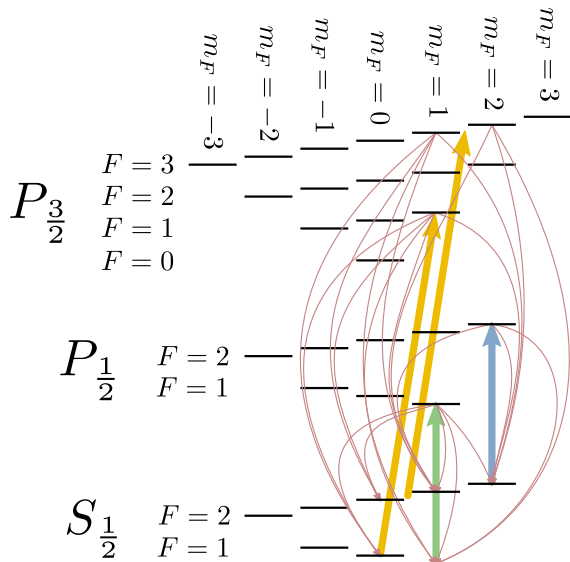


Figure 5.7: The full cooling scheme, including repump lasers (yellow), cooling lasers (blue and green), and all possible decay paths (red). The repump beam which is drawn in between two ground and excited states has a frequency equal to the average of those two transitions.

started. Again, out atom now sees no light, but which laser has zero intensity and which targets the wrong transition are swapped.

As our atom continues rightward, it now has to contend with the potential hill formed by the ω_2 laser, and is most likely to undergo spontaneous emission from the $|2, 2\rangle$ excited state near the top of the potential hill. This time emission is most likely to put the atom into the $|1, 1\rangle$ groundstate.

This process repeats, with atoms repeatedly climbing potential hills and being cooled. They spend approximately half their time in the $|1, 1\rangle$ groundstate, allowing us to take advantage of the strong interspecies repulsion that that state entails for our two atomic species.

Of course, as is always the case, things aren't that simple. Whilst the two spontaneous decays mentioned above are the most likely, they are by no means the only possibilities. Some spontaneous decays will put the atoms back into the groundstate from which they came, with no harm done except a little extra heating from the photon recoil. Other decays however will put our atom into states that are not involved in the cooling scheme, where they will remain with no further cooling unless we do something about it. For this we need repump lasers (Figure 5.7).

There are three states that the atom might end up in as a result of decay from the two excited states involved in the cooling process, and two repump lasers are used to excite them to three $P_{3/2}$ states. Two of these transitions are similar enough that they can be addressed with the same laser.

5.5.2 Methods

The cooling scheme was simulated for the case of a single atom, with the internal state of the atom modelled with the Schrödinger equation in the eigenbasis of the Hyperfine and Zeeman Hamiltonians (described in Section 2.3), the state vector being a complex 32-vector⁴. The dipole transition matrix elements coupling each pair of states were

⁴One complex number for each state in Figure 5.7.

```
rev:    168 (eb2975e06a08)
author: chrisjbillington
date:   Tue Jun 19 17:15:34 2018 +1000
summary: Editing velocimetry
```

each computed as the appropriate linear sum of the dipole matrix elements at zero field, using the dipole approximation and the rotating wave approximation, as described in Section 2.3.5. Since the corresponding Rabi frequencies depend on the laser intensity as well as the dipole matrix elements, they are functions of space, to be computed at each integration timestep as the atom moves through different intensities of the cooling beams. Following [2, p 4], this produced a set of 32 coupled differential equations for the complex amplitudes of each state, of the form :

$$i\hbar \frac{d}{dt} c_e(t) = -\frac{1}{2} e \sum_{g,n} E_n \langle g|q_n|e\rangle c_g(t) e^{-i\delta_{nge}t}, \quad (5.2)$$

and

$$i\hbar \frac{d}{dt} c_g(t) = -\frac{1}{2} e \sum_{e,n} E_n \langle g|q_n|e\rangle c_e(t) e^{i\delta_{nge}t}, \quad (5.3)$$

where each $c(t)$ is the complex amplitude of one state; the e indices are over the excited states and the g indices over the groundstates; the n indices are over the lasers, with E_n being the amplitude of the n^{th} laser's electric field, δ_{nge} the detuning of the n^{th} laser from the transition between the g^{th} ground and e^{th} excited states, and $\langle g|q_n|e\rangle$ the dipole moment between the g^{th} ground and e^{th} excited states for the polarisation of the n^{th} laser.

The external motion of the atom was modelled classically, with the atom having a definite position and velocity in one dimension. The force on the atom was computed from the dipole forces that the two groundstates involved in the cooling cycle experience due to the standing waves formed by the cooling beams. An expectation value of the dipole force was computed as:

$$\langle F \rangle = |\langle 1, 1 | \Psi \rangle|^2 F_{|1,1\rangle} + |\langle 2, 2 | \Psi \rangle|^2 F_{|2,2\rangle}, \quad (5.4)$$

where $F_{|1,1\rangle}$ and $F_{|2,2\rangle}$ are the dipole forces on the two groundstates, calculated using [2, eqn 3.16, p 33] with one standing wave offset from the other by a quarter wavelength. The forces on other groundstates are neglected since the repump beams do not have intensity gradients, and since the cooling beams are much further away from resonance for groundstates other than the two in the cooling cycle. Forces on excited states are also neglected—although the forces on the two excited states in the cooling cycle are not smaller than those on the corresponding groundstates, the excited state populations are small since the cooling beams are several linewidths away from resonance.

This expectation value of the dipole force was used to model the classical motion of the atom. Although the components of an atom in superposition would in reality spatially separate under the influence of a force that is different for different internal states of the atom, as in the Stern-Gerlach experiment, our atom only transitions between the two states subject to different forces via spontaneous emission, after which it is in an eigenstate. Accordingly, the expectation value calculation is always dominated by one of the two groundstates and the potential for Stern-Gerlach separation does not arise.

Spontaneous emission was simulated stochastically at each integration timestep, with probability of decay per unit time equal to the sum of populations in all excited states, multiplied by their decay rates (equal to the natural linewidths of each of the two fine-structure lines). Multiplying by the duration of one timestep, and comparing with a random number then determined whether a decay was to occur.

In the event of a decay, one excited state was randomly chosen with probability proportional to its population, and then one groundstate, weighted by the transition strengths from the excited state. All population was then put into that groundstate and the simulation continued, with one photon's worth of momentum in a random 1D direction added to the atom's momentum to account for photon recoil.

Type	Transition(s) targeted	Detuning	Intensity (per beam)	Polarisation
cooling (standing wave)	$ S_{\frac{1}{2}}, 2, 2\rangle \rightarrow P_{\frac{1}{2}}, 2, 2\rangle$	+ 66.6 MHz	5.0 mW cm ⁻²	π
cooling (standing wave)	$ S_{\frac{1}{2}}, 1, 1\rangle \rightarrow P_{\frac{1}{2}}, 1, 1\rangle$	+ 31.9 MHz	5.0 mW cm ⁻²	π
repump (single beam)	$ S_{\frac{1}{2}}, 2, 1\rangle \rightarrow P_{\frac{3}{2}}, 2, 2\rangle$ $ S_{\frac{1}{2}}, 2, 0\rangle \rightarrow P_{\frac{3}{2}}, 2, 1\rangle$	Midway between	50.0 mW cm ⁻²	σ^+
repump (single beam)	$ S_{\frac{1}{2}}, 1, 0\rangle \rightarrow P_{\frac{3}{2}}, 1, 1\rangle$	0	10.0 mW cm ⁻²	σ^+

Table 5.1: The parameters used in the laser cooling simulations. There are four lasers, each with a specified polarisation, intensity, and detuning from the transition it targets.

The equations of motion were solved using fourth order Runge–Kutta integration (Section ??)

5.5.3 Results

The laser parameters used in the simulation are shown in Table 5.1. The magnetic field strength used was 34 G.

The simulation was run for 715 million integration timesteps of 20 picoseconds each⁵, for a total of 14.3 milliseconds of simulation time. This took 14 days of computer time. In that time, the atom moved a maximum distance of 26 micrometres from its starting position, and its final position was 790 nanometres from its starting position. The atom's initial velocity was 195 millimetres per second, and during the simulation it reversed the direction of its velocity 2226 times. 4103 photons were emitted, for an average scattering rate of 2.87×10^5 photons per second.

Computing the time averaged energy of the atom over the whole simulation using:

$$\langle E \rangle = \frac{1}{2} m_{\text{Rb}} \langle v^2 \rangle, \quad (5.5)$$

and converting to temperature units with $k_B T = \langle E \rangle$ gives a temperature of 8.1 μK . Since this is only a one-dimensional simulation, a temperature approximately three times higher would be expected in three dimensions, as the atom would have approximately the same amount of energy in each spatial degree of freedom.

A histogram of what fraction of the time the atom spent at different velocities is shown in Figure 5.8.

This one-dimensional temperature corresponds to approximately 44 recoil energies, and if extrapolated to three dimensions, about 132 recoils. Given that the potassium vortex potentials are at most about 15 recoils deep without a Feshbach resonance, and only about 8 recoils when you consider that the rubidium is not in the ideal state half of the time, this result will only be able to keep rubidium atoms trapped in vortex cores if we can get a factor of 20 or so increase in the interspecies repulsion via a Feshbach resonance.

This simulation has not, however, been optimised. Whilst some parameters were computed from others based on assumptions about optimal scattering rates and the like, no attempt has been made to scan over parameter space to see if the temperature can be made lower. I plan on using a genetic algorithm to optimise the parameters by managing a population of simulations running on one of the university clusters. A significant speed up should be possible by excluding from the simulation the atomic states that were shown in the first run never to become occupied. This will eliminate approximately two thirds

⁵Which is about ten timesteps per oscillation of the fastest oscillating terms, which oscillate at a rate equal to approximately half the 6.8GHz hyperfine splitting of the rubidium groundstates.

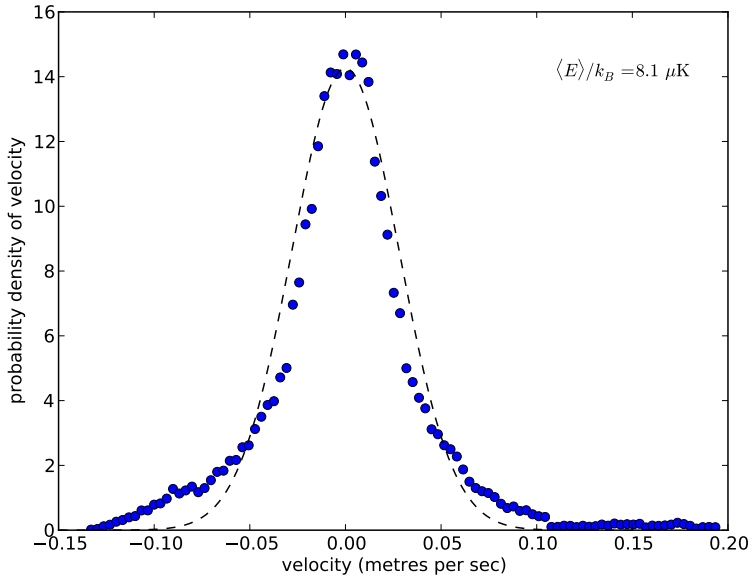


Figure 5.8: Histogram of atom velocity over time, normalised such that it can be interpreted as a probability density. A best-fit Maxwell-Boltzmann distribution is shown as the dotted line. It is no surprise that it is not a good fit—there is no thermalisation happening since we have only one atom and no collisions. The average energy is more informative than the fit parameters for determining the temperature that an ensemble of such atoms would have if they were allowed to thermalise. This is because the average energy would stay constant throughout thermalisation, whereas the fit parameters would not. Only for a fully thermal distribution would the two methods agree. The long tail visible to the right is the atom's initial slowdown from its starting velocity.

of the states, and since the simulation is quadratic in the number of states, this should provide an approximately 10× increase in simulation speed.

The simulation will also require repetition to verify that the results still hold when a significant error, recently discovered, is corrected. The error is that the Zeeman sublevels used in the simulation were all incorrect by a sign. There is a large degree of symmetry with this change, and the scattering rates between all involved states are almost identical, so I am confident that this will only slightly change the results.

Ultimately only experimentation will show whether this method is viable, and what the optimal parameters are, but since it requires a large number of lasers, it is likely worth further theoretical investigation before attempting to implement it.

5.5.4 Vortex-assisted Sisyphus cooling

[COMMENT ON HIDDEN VARIABLES - PRESENTED HERE TO MAKE A POINT]

Another idea for a cooling scheme is to use the vortex potential itself as a spatial discriminator for transferring atoms between states. Similar to how a MOT traps atoms by bringing them into resonance with optical pumping only when they are some distance from the trap's centre, we could use the shape of the vortex potential to bring an RF or

```
rev:    168 (eb2975e06a08)
author: chrisjbillington
date:   Tue Jun 19 17:15:34 2018 +1000
summary: Editing velocimetry
```

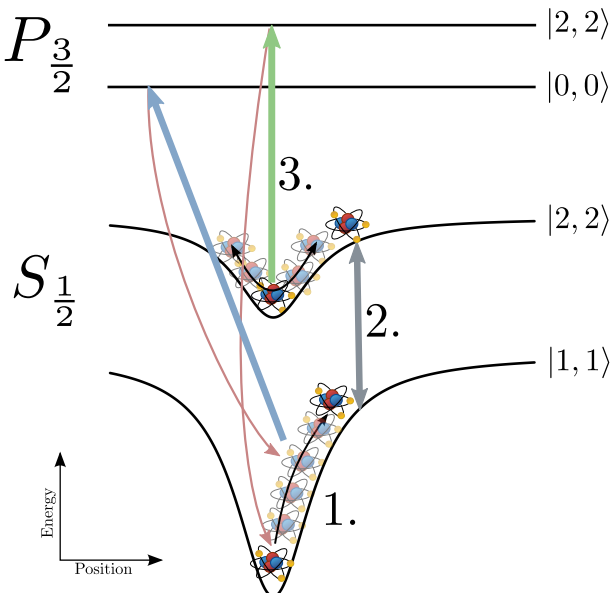


Figure 5.9: A basic description of the vortex-assisted cooling scheme.

1. The rubidium atom in its $|1, 1\rangle$ groundstate repeatedly scatters photons from the laser marked with the blue arrow, climbing the vortex potential as it does so. The optical transition's linewidth is large enough that the energy shift due to the vortex potential does not move it off resonance.
2. An RF or microwave transition however, has an extremely narrow linewidth; its effective linewidth is dependent only on the RF/microwave power. A microwave transition (grey arrow) comes into resonance only when the atom moves sufficiently far from the vortex core's centre, and coherently transfers population into the $|2, 2\rangle$ groundstate.
3. The atom oscillates back and forth in the much shallower vortex potential that its $|2, 2\rangle$ groundstate experiences. It is pumped weakly by the laser marked with the green arrow, and after a random time delay (and hence at a random position) spontaneously decays back to the $|1, 1\rangle$ groundstate.

microwave transition into resonance only when trapped tracer particles are some way up the side of a vortex core.

The basic idea is outlined in Figure 5.9. In the presence of the Feshbach resonance, atoms in the $|1, 1\rangle$ state will scatter some tens of photons, using whichever transition is most likely to have them decay to the same groundstate with minimal repumping (transitioning to the $|0, 0\rangle$ excited state on the D_2 line looks to be the best choice). As the atom scatters photons, it climbs the side of the vortex potential, converting its new found kinetic energy (from photon recoil) into potential energy.

Due to the state-dependence of the interspecies scattering length, the vortex potentials for different states have different depths. This means that the RF or microwave frequency required to transition between the different hyperfine states and Zeeman sublevels varies as a function of space, and can be tuned so as to only be resonant with atoms which have nearly escaped the vortex core.

The atom is then transferred into a different hyperfine or Zeeman state (the $|2, 2\rangle$ groundstate should suit) and the hope is that it then lacks the kinetic energy to escape the (shallower) vortex potential it now finds itself in. Rather, it will oscillate back and forth in the well until a weak laser pumps it back into the $|1, 1\rangle$ groundstate via spontaneous emission from some excited state (again chosen to maximise the decay probability to

$|1, 1\rangle$; the $|2, 2\rangle P_{\frac{3}{2}}$ excited state looks to be a good choice.)

If this goes to plan, statistically the atom will be closer to the center of the $|1, 1\rangle$ vortex potential than when it left. Provided its corresponding drop in potential energy makes up for all the photon scattering (which provides fluorescence imaging), then we have a cooling scheme. It is yet another Sisyphus effect, with the atom climbing steep vortex potential hills and descending shallower ones.

This scheme will be simulated to determine its viability; preliminary calculations haven't turned up any problems yet.

References

- [1] D. J. Wineland, R. E. Drullinger, and F. L. Walls. *Radiation-Pressure Cooling of Bound Resonant Absorbers*. Physical Review Letters **40**, 1639 (1978).
DOI: [10.1103/PhysRevLett.40.1639](https://doi.org/10.1103/PhysRevLett.40.1639). [p 1]
- [2] H. J. Metcalf and P. V. der Straten. *Laser Cooling and Trapping*. Springer (1999). [pp 2, 6, 15, 32, and 34]
- [3] E. L. Raab, M. Prentiss, A. Cable, S. Chu, and D. E. Pritchard. *Trapping of Neutral Sodium Atoms with Radiation Pressure*. Physical Review Letters **59**, 2631 (1987).
DOI: [10.1103/PhysRevLett.59.2631](https://doi.org/10.1103/PhysRevLett.59.2631). [p 2]
- [4] P. Zeeman. *On the influence of magnetism on the nature of the light emitted by a substance*. Philosophical Magazine Series 5 **43**, 226 (1897). [pp 2 and 10]
- [5] D. M. Brink and C. V. Sukumar. *Majorana spin-flip transitions in a magnetic trap*. Physical Review A **74**, 035401 (2006). DOI: [10.1103/PhysRevA.74.035401](https://doi.org/10.1103/PhysRevA.74.035401). [pp 2 and 3]
- [6] A. Ashkin. *Acceleration and Trapping of Particles by Radiation Pressure*. Physical Review Letters **24**, 156 (1970). DOI: [10.1103/PhysRevLett.24.156](https://doi.org/10.1103/PhysRevLett.24.156). [p 3]
- [7] J. Dalibard and C. Cohen-Tannoudji. *Laser cooling below the Doppler limit by polarization gradients: Simple theoretical models*. JOSA B **6**, 2023 (1989).
DOI: [10.1364/JOSAB.6.002023](https://doi.org/10.1364/JOSAB.6.002023). [p 3]
- [8] P. J. Ungar, D. S. Weiss, E. Riis, and S. Chu. *Optical molasses and multilevel atoms: Theory*. Journal of the Optical Society of America B **6**, 2058 (1989).
DOI: [10.1364/JOSAB.6.002058](https://doi.org/10.1364/JOSAB.6.002058). [p 3]
- [9] P. D. Lett, W. D. Phillips, S. L. Rolston, C. E. Tanner, R. N. Watts, and C. I. Westbrook. *Optical molasses*. Journal of the Optical Society of America B **6**, 2084 (1989). DOI: [10.1364/JOSAB.6.002084](https://doi.org/10.1364/JOSAB.6.002084). [p 3]
- [10] C. Salomon, J. Dalibard, W. D. Phillips, A. Clairon, and S. Guellati. *Laser Cooling of Cesium Atoms Below 3 μK*. Europhysics Letters (EPL) **12**, 683 (1990).
DOI: [10.1209/0295-5075/12/8/003](https://doi.org/10.1209/0295-5075/12/8/003). [p 3]
- [11] H. F. Hess. *Evaporative cooling of magnetically trapped and compressed spin-polarized hydrogen*. Physical Review B **34**, 3476 (1986).
DOI: [10.1103/PhysRevB.34.3476](https://doi.org/10.1103/PhysRevB.34.3476). [p 3]

rev: 168 (eb2975e06a08)
author: chrisjbillington
date: Tue Jun 19 17:15:34 2018 +1000
summary: Editing velocimetry

- [12] M. H. Anderson, J. R. Ensher, M. R. Matthews, C. E. Wieman, and E. A. Cornell. *Observation of Bose–Einstein Condensation in a Dilute Atomic Vapor*. *Science* **269**, 198 (1995). DOI: [10.1126/science.269.5221.198](https://doi.org/10.1126/science.269.5221.198). [p 3]
- [13] Y.-J. Lin, A. R. Perry, R. L. Compton, I. B. Spielman, and J. V. Porto. *Rapid production of ^{87}Rb Bose–Einstein condensates in a combined magnetic and optical potential*. *Physical Review A* **79**, 063631 (2009). DOI: [10.1103/PhysRevA.79.063631](https://doi.org/10.1103/PhysRevA.79.063631). [p 4]
- [14] C. Chin, R. Grimm, P. Julienne, and E. Tiesinga. *Feshbach resonances in ultracold gases*. *Reviews of Modern Physics* **82**, 1225 (2010). DOI: [10.1103/RevModPhys.82.1225](https://doi.org/10.1103/RevModPhys.82.1225). [p 4]
- [15] S. Inouye, M. R. Andrews, J. Stenger, H.-J. Miesner, D. M. Stamper-Kurn, and W. Ketterle. *Observation of Feshbach resonances in a Bose–Einstein condensate*. *Nature* **392**, 151 (1998). DOI: [10.1038/32354](https://doi.org/10.1038/32354). [p 4]
- [16] G. Thalhammer, G. Barontini, L. De Sarlo, J. Catani, F. Minardi, and M. Inguscio. *Double Species Bose–Einstein Condensate with Tunable Interspecies Interactions*. *Physical Review Letters* **100**, 210402 (2008). DOI: [10.1103/PhysRevLett.100.210402](https://doi.org/10.1103/PhysRevLett.100.210402). [pp 5 and 31]
- [17] E. Madelung. *Quantentheorie in hydrodynamischer Form*. *Zeitschrift für Physik A Hadrons and Nuclei* **40**, 322 (1927). DOI: [10.1007/BF01400372](https://doi.org/10.1007/BF01400372). [p 5]
- [18] D. A. Steck. *Rubidium 87 D Line Data*, (2015). (revision 2.1.4) <http://steck.us/alkalidata>. [pp 6, 7, 10, 11, 14, 19, and 20]
- [19] D. A. Steck. *Quantum and Atom Optics*, (2017). (revision 0.12.0) <http://steck.us/teachinng>. [pp 6, 15, 16, 18, and 20]
- [20] B. E. King. *Angular Momentum Coupling and Rabi Frequencies for Simple Atomic Transitions*. arXiv:0804.4528 [physics] (2008). ARXIV: [0804.4528](https://arxiv.org/abs/0804.4528). [pp 6 and 16]
- [21] P. M. Farrell and W. R. MacGillivray. *On the consistency of Rabi frequency calculations*. *Journal of Physics A: Mathematical and General* **28**, 209 (1995). DOI: [10.1088/0305-4470/28/1/023](https://doi.org/10.1088/0305-4470/28/1/023). [p 6]
- [22] E. Arimondo, M. Inguscio, and P. Violino. *Experimental determinations of the hyperfine structure in the alkali atoms*. *Rev. Mod. Phys.* **49**, 31 (1977). DOI: [10.1103/RevModPhys.49.31](https://doi.org/10.1103/RevModPhys.49.31). [p 7]
- [23] J. J. Sakurai. *Modern Quantum Mechanics*. Pearson (1994). [p 8]
- [24] G. Breit and I. I. Rabi. *Measurement of Nuclear Spin*. *Physical Review* **38**, 2082 (1931). DOI: [10.1103/PhysRev.38.2082.2](https://doi.org/10.1103/PhysRev.38.2082.2). [p 15]
- [25] G. P. Bewley. *The generation of particles to observe quantized vortex dynamics in superfluid helium*. *Cryogenics* **49**, 549 (2009). DOI: [10.1016/j.cryogenics.2008.10.018](https://doi.org/10.1016/j.cryogenics.2008.10.018). [p 23]
- [26] G. P. Bewley, D. P. Lathrop, and K. R. Sreenivasan. *Superfluid Helium: Visualization of quantized vortices*. *Nature* **441**, 588 (2006). DOI: [10.1038/441588a](https://doi.org/10.1038/441588a). [p 23]
- [27] R. E. Packard. *Vortex photography in liquid helium*. *Physica B+C* **109–110**, 1474 (1982). DOI: [10.1016/0378-4363\(82\)90171-1](https://doi.org/10.1016/0378-4363(82)90171-1). [p 23]

rev: 168 (eb2975e06a08)

author: chrisjbillington

date: Tue Jun 19 17:15:34 2018 +1000

summary: Editing velocimetry

- [28] W. S. Bakr, J. I. Gillen, A. Peng, S. F. Illing, and M. Greiner. *A quantum gas microscope for detecting single atoms in a Hubbard-regime optical lattice*. Nature **462**, 74 (2009). DOI: [10.1038/nature08482](https://doi.org/10.1038/nature08482). [p 23]
- [29] B. P. Anderson, P. C. Haljan, C. A. Regal, D. L. Feder, L. A. Collins, C. W. Clark, and E. A. Cornell. *Watching Dark Solitons Decay into Vortex Rings in a Bose-Einstein Condensate*. Physical Review Letters **86**, 2926 (2001). DOI: [10.1103/PhysRevLett.86.2926](https://doi.org/10.1103/PhysRevLett.86.2926). [p 24]
- [30] V. Bretin, P. Rosenbusch, F. Chevy, G. V. Shlyapnikov, and J. Dalibard. *Quadrupole Oscillation of a Single-Vortex Bose-Einstein Condensate: Evidence for Kelvin Modes*. Physical Review Letters **90**, 100403 (2003). DOI: [10.1103/PhysRevLett.90.100403](https://doi.org/10.1103/PhysRevLett.90.100403). [p 24]
- [31] M. Leadbeater, T. Winiecki, D. C. Samuels, C. F. Barenghi, and C. S. Adams. *Sound Emission due to Superfluid Vortex Reconnections*. Physical Review Letters **86**, 1410 (2001). DOI: [10.1103/PhysRevLett.86.1410](https://doi.org/10.1103/PhysRevLett.86.1410). [p 24]
- [32] C. N. Weiler, T. W. Neely, D. R. Scherer, A. S. Bradley, M. J. Davis, and B. P. Anderson. *Spontaneous vortices in the formation of Bose-Einstein condensates*. Nature **455**, 948 (2008). DOI: [10.1038/nature07334](https://doi.org/10.1038/nature07334). [p 24]
- [33] D. V. Freilich, D. M. Bianchi, A. M. Kaufman, T. K. Langin, and D. S. Hall. *Real-Time Dynamics of Single Vortex Lines and Vortex Dipoles in a Bose-Einstein Condensate*. Science **329**, 1182 (2010). DOI: [10.1126/science.1191224](https://doi.org/10.1126/science.1191224). [p 24]
- [34] S. W. Hawking. *A Brief History of Time: From the Big Bang to Black Holes*. Bantam Books (1988). [p 24]
- [35] S. Corrsin. *Turbulent Flow*. American Scientist **49**, 300 (1961). [p 24]
- [36] P. A. Davidson. *Turbulence: An Introduction for Scientists and Engineers*. Oxford University Press (2004). [p 25]
- [37] A. Kolmogorov. *The Local Structure of Turbulence in Incompressible Viscous Fluid for Very Large Reynolds' Numbers*. Akademiia Nauk SSSR Doklady **30**, 301 (1941). [p 25]
- [38] D. B. Spalding. *Kolmogorov's Two-Equation Model of Turbulence*. Proceedings of the Royal Society of London. Series A: Mathematical and Physical Sciences **434**, 211 (1991). DOI: [10.1098/rspa.1991.0089](https://doi.org/10.1098/rspa.1991.0089). [p 25]
- [39] L. F. Richardson. *Weather Prediction by Numerical Process*. Cambridge University Press (2007). (First published 1922). [p 25]
- [40] M. Tsubota and M. Kobayashi. *Energy Spectra of Quantum Turbulence*. In *Progress in Low Temperature Physics: Quantum Turbulence*, volume 16, pages 1–43. Elsevier (2009). [p 25]
- [41] W. F. Vinen. *How is turbulent energy dissipated in a superfluid?* Journal of Physics: Condensed Matter **17**, S3231 (2005). DOI: [10.1088/0953-8984/17/45/006](https://doi.org/10.1088/0953-8984/17/45/006). [p 25]
- [42] L. Onsager. *Statistical hydrodynamics*. Il Nuovo Cimento (1943-1954) **6**, 279 (1949). DOI: [10.1007/BF02780991](https://doi.org/10.1007/BF02780991). [p 25]
- [43] R. H. Kraichnan. *Inertial Ranges in Two-Dimensional Turbulence*. Physics of Fluids **10**, 1417 (1967). DOI: [doi:10.1063/1.1762301](https://doi.org/10.1063/1.1762301). [p 25]

rev: 168 (eb2975e06a08)
author: chrisjbillington
date: Tue Jun 19 17:15:34 2018 +1000
summary: Editing velocimetry

- [44] T. Simula, M. J. Davis, and K. Helmerson. *Emergence of Order from Turbulence in an Isolated Planar Superfluid*. Physical Review Letters **113**, 165302 (2014). DOI: [10.1103/PhysRevLett.113.165302](https://doi.org/10.1103/PhysRevLett.113.165302). [p 25]
- [45] A. J. Groszek, M. J. Davis, D. M. Paganin, K. Helmerson, and T. P. Simula. *Vortex Thermometry for Turbulent Two-Dimensional Fluids*. Physical Review Letters **120**, 034504 (2018). DOI: [10.1103/PhysRevLett.120.034504](https://doi.org/10.1103/PhysRevLett.120.034504). [p 25]
- [46] S. P. Johnstone, A. J. Groszek, P. T. Starkey, C. J. Billington, T. P. Simula, and K. Helmerson. *Order from chaos: Observation of large-scale flow from turbulence in a two-dimensional superfluid*. arXiv:1801.06952 [cond-mat, physics:physics] (2018). ARXIV: [1801.06952](https://arxiv.org/abs/1801.06952). [p 25]
- [47] G. Gauthier, M. T. Reeves, X. Yu, A. S. Bradley, M. Baker, T. A. Bell, H. Rubinsztein-Dunlop, M. J. Davis, and T. W. Neely. *Negative-Temperature Onsager Vortex Clusters in a Quantum Fluid*. arXiv:1801.06951 [cond-mat, physics:physics] (2018). ARXIV: [1801.06951](https://arxiv.org/abs/1801.06951). [p 25]
- [48] A. J. Leggett. *Superfluidity*. Reviews of Modern Physics **71**, S318 (1999). DOI: [10.1103/RevModPhys.71.S318](https://doi.org/10.1103/RevModPhys.71.S318). [p 25]
- [49] A. J. Leggett. *Quantum Liquids: Bose Condensation and Cooper Pairing in Condensed-Matter Systems*. Oxford University Press (2006). [p 26]
- [50] C. J. Billington. *Particle Velocimetry of Vortices in Bose-Einstein Condensates*. Honours thesis, Monash University (2010). [pp 27, 28, 29, and 30]

rev: 168 (eb2975e06a08)
author: chrisjbillington
date: Tue Jun 19 17:15:34 2018 +1000
summary: Editing velocimetry

Word count

Total

Words in text: 65389
Words in headers: 516
Words outside text (captions, etc.): 10708
Number of headers: 137
Number of floats/tables/figures: 51
Number of math inlines: 1979
Number of math displayed: 322

Files: 8

Subcounts:

```
text+headers+captions (#headers/#floats/#inlines/#displayed)
7422+77+1300 (23/3/559/73) File(s) total: atomic_physics.tex
50+0+0 (0/0/0/0) File(s) total: front_matter.tex
16752+117+3154 (32/14/478/107) File(s) total: hidden_variables.tex
2721+14+98 (4/0/16/0) File(s) total: introduction.tex
23088+155+3403 (31/15/824/137) File(s) total: numerics.tex
9497+81+1478 (26/5/7/0) File(s) total: software.tex
5075+37+890 (12/10/88/5) File(s) total: velocimetry.tex
784+35+385 (9/4/7/0) File(s) total: wave_mixing.tex
```

rev: 168 (eb2975e06a08)
author: chrisjbillington
date: Tue Jun 19 17:15:34 2018 +1000
summary: Editing velocimetry